



## 저작자표시-비영리-변경금지 2.0 대한민국

이용자는 아래의 조건을 따르는 경우에 한하여 자유롭게

- 이 저작물을 복제, 배포, 전송, 전시, 공연 및 방송할 수 있습니다.

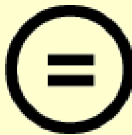
다음과 같은 조건을 따라야 합니다:



저작자표시. 귀하는 원저작자를 표시하여야 합니다.



비영리. 귀하는 이 저작물을 영리 목적으로 이용할 수 없습니다.



변경금지. 귀하는 이 저작물을 개작, 변형 또는 가공할 수 없습니다.

- 귀하는, 이 저작물의 재이용이나 배포의 경우, 이 저작물에 적용된 이용허락조건을 명확하게 나타내어야 합니다.
- 저작권자로부터 별도의 허가를 받으면 이러한 조건들은 적용되지 않습니다.

저작권법에 따른 이용자의 권리는 위의 내용에 의하여 영향을 받지 않습니다.

이것은 [이용허락규약\(Legal Code\)](#)을 이해하기 쉽게 요약한 것입니다.

[Disclaimer](#)

공학박사학위논문

Effect of pressure on the film  
deposition during RF magnetron  
sputtering considering charged  
nanoparticles

RF 마그네트론 스퍼터링 내에서 압력에 따른  
하전된 나노입자의 생성과 압력에 따른 박막 증착  
거동 차이

2021년 2월

서울대학교 대학원

재료공학부

김 두 윤

# Effect of pressure on the film deposition during RF magnetron sputtering considering charged nanoparticles

지도교수 황 농 문

이 논문을 공학박사 학위논문으로 제출함

2021 년 2월

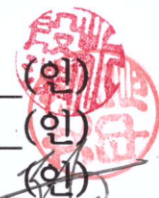
서울대학교 대학원

재료공학부

김 두 윤

김두윤의 공학박사 학위논문을 인준함  
2021년 2월

위 원 장	박 은 수	(인)
부위원장	황 농 문	(인)
위 원	장 호 원	(인)
위 원	김 근 수	(인)
위 원	나 태 옥	(인)



# Abstract

## Effect of pressure on the film deposition during RF magnetron sputtering considering charged nanoparticles

Du Yun Kim

Department of Materials Science and Engineering

The Graduate School

Seoul National University

Non-classical crystallization, in which charged nanoparticles (NPs) are building blocks of film growth, has been extensively studied in chemical vapor deposition. It is necessary to study the non-classical crystallization in physical vapor deposition. Thus, generation of NPs in physical vapor deposition, especially in radio frequency (RF) magnetron sputtering using titanium (Ti) was confirmed and possibility of being charged was investigated. Also, the effect of charged NPs on film deposition was analyzed. The Ti NPs were captured on amorphous carbon membranes by means of

exposing the membranes to plasma for a few seconds and they were examined by transmission electron microscopy (TEM). The NPs with the size of  $\sim 4$  nm were observed and confirmed to be Ti. Also, the possibility of being charged was investigated by applying additional electric bias of  $-70$ ,  $0$ ,  $+5$ ,  $+15$  and  $+30$  V to the membranes. The number density of Ti NPs was increased with increasing negative bias, whereas decreased with positive bias. It showed that these Ti NPs were positively charged. Under the same condition and experimental setting, Ti films were deposited on silicon substrates with the substrate bias of  $-70$ ,  $0$ ,  $+30$  V. Film quality was analyzed by TEM, field-emission scanning electron microscopy (FESEM), X-ray diffraction (XRD) and X-ray reflectivity (XRR). Compared to the film deposited with  $0$  V, the film deposited at  $-70$  V had the highest crystallinity, growth rate and density, whereas the film deposited with  $+30$  V had the lowest crystallinity, growth and density. This difference came from the number density difference of charged Ti NPs to each substrate. It can be confirmed that the control of the number density of charged Ti NPs is necessary to enhance the film quality deposited at room temperature.

Also, the effect of pressure on the generation of Ti NPs and on the film deposition was investigated. Ti NPs were captured on amorphous TEM membranes with the electric biases of  $-30$ ,  $0$ ,  $+50$  V under various pressure. The number density of Ti NPs was also

examined by TEM, which was increased with negative bias, whereas decreased with positive bias. As the pressure increased, the difference of number density with the electric bias also increased. This showed that the ratio of charged to neutral Ti NPs increased as the pressure increased. Ti films were deposited under the same condition and experimental setting and analyzed by FESEM and XRD. The effect of substrate bias on film growth rate became more pronounced as the pressure increased. This sensitive dependence of the film growth rate on the substrate bias under higher pressure is in agreement with the sensitive dependence of the number density of Ti NPs on the substrate bias under higher pressure.

This understanding of generation of charged NPs during RF magnetron sputtering was also applied to deposition of tungsten film with the purpose of decreasing resistivity of the film. Tungsten film was deposited with substrate bias of  $-70$ ,  $-30$ ,  $-10$ ,  $0$ ,  $+50$  V under various pressure. Resistivity of tungsten film decreased with negative substrate bias, whereas increased with positive substrate bias. This bias effect on resistivity became pronounced as the pressure increased. This difference should be attributed to the attraction and repelling of charged NPs to the substrate by the substrate bias. Therefore, it can be said that the charge of NPs play an important role to obtain low resistivity film. In this point of view, high power impulse magnetron sputtering (HiPIMS) was used to

make NPs to be charged further, which resulted from the higher ionization ratio. The tungsten films prepared by HiPIMS showed much higher growth rate than RF magnetron sputtering with comparable resistivity. It can be predicted that the film with lower resistivity with high growth rate can be obtained by HiPIMS when optimizing process condition and introducing additional experimental setting.

**Keyword :** Charged nanoparticle, RF magnetron sputtering, Titanium thin film, Tungsten thin film, HiPIMS

**Student Number :** 2016–20772

# List of Figures

**Figure 1.1.** (a) Diamond and (b) soot grown on Si and Fe substrates, respectively [7, 13].

**Figure 1.2.** Number concentrations and size distributions of negatively (open) and positively (closed) charged NPs at a N<sub>2</sub> flow rate of 500 sccm and 1000 sccm, respectively [17].

**Figure 1.3.** FESEM images of (a) low and (b) high magnification images of a floating substrate and (c) low and (d) high magnification images of a grounded substrate with a N<sub>2</sub> flow rate of 500 sccm [17].

**Figure 1.4.** FESEM images of (a) top and (b) cross-section view images of a floating substrate and (c) top and (d) cross-section view images of a grounded substrate with a N<sub>2</sub> flow rate of 1000 sccm [17].

**Figure 1.5.** Phenomena on the target surface by ion bombardment.

**Figure 1.6.** Glow discharge formation inside the vacuum chamber for generating the energetic particles.

**Figure 1.7.** Schematics of a conventional DC sputtering system.

**Figure 1.8.** Schematics of a conventional DC magnetron sputtering system.

**Figure 2.1.** Schematics of RF sputtering system (a) main chamber (b) grounded mesh.



**Figure 2.2.** STEM images of NPs captured on amorphous carbon TEM membranes at the electric bias of (a)  $-70$  V (b)  $0$  V (c)  $+5$  V (d)  $+15$  V and (e)  $+30$  V.

**Figure 2.3.** HRTEM images and fast Fourier transform (FFT) information (inset of the lower right in the image) with d-spacing value of NPs at the electric bias with (a)  $-70$  V and (b)  $0$  V.

**Figure 2.4.** SEM images of Ti films deposited on Si substrates at the electric bias of (a)  $-70$  V (b)  $0$  V and (c)  $+30$  V.

**Figure 2.5.** Low and high magnification TEM images with FFT information (the lower right) of the Ti films deposited on Si substrates at the electric bias of (a), (d)  $-70$  V (b), (e)  $0$  V and (c), (f)  $+30$  V.

**Figure 2.6.** Diffraction pattern images of the Ti films at the electric bias of (a)  $-70$  V (b)  $0$  V and (c)  $+30$  V.

**Figure 2.7.** X-ray reflectivity (XRR) data of the Ti films in the range of  $0^\circ \sim 0.7^\circ$  at the electric bias of  $-70$  V,  $0$  V and  $+30$  V.

**Figure 3.1.** Schematics of RF sputtering system (a) main chamber (b) grounded mesh.

**Figure 3.2.** HRTEM images and FFT information (inset of the lower right in the image) with d-spacing value of NPs at the substrate bias of  $0$  V under (a)  $20$  mTorr and (b)  $80$  mTorr.

**Figure 3.3.** HRTEM images of NPs at the substrate bias of (a)  $-30$  V, (b)  $0$  V and (c)  $+50$  V under  $20$  mTorr and (d)  $-30$  V, (e)  $0$  V and (f)  $+50$  V under  $80$  mTorr.

**Figure 3.4.** SEM images of the Ti films deposited on Si substrates under 80 mTorr at biases of (a)  $-30$  V (b)  $-10$  V (c)  $0$  V and (d)  $+50$  V.

**Figure 3.5.** Growth rate of the Ti films deposited at the substrate bias of  $-30$  V,  $-10$  V,  $0$  V and  $+50$  V under 20 mTorr, 40 mTorr, 60 mTorr and 80 mTorr.

**Figure 3.6.** XRD data of the Ti films deposited at the substrate bias of  $-30$  V,  $-10$  V,  $0$  V and  $+50$  V under (a) 20 mTorr, (b) 40 mTorr, (c) 60 mTorr and (d) 80 mTorr.

**Figure 4.1.** Crystal structure of A-15  $\beta$  tungsten.

**Figure 4.2.** Schematics of RF sputtering system (a) main chamber (b) grounded mesh.

**Figure 4.3.** Schematics of HiPIMS system.

**Figure 4.4.** Resistivity of the films deposited by RF magnetron sputtering under 5 mTorr, 20 mTorr and 80 mTorr.

**Figure 4.5.** Enlarged graph of the resistivity of the films deposited by RF magnetron sputtering under 5 mTorr, 20 mTorr and 80 mTorr.

**Figure 4.6.** XRD of the films deposited by RF magnetron sputtering under (a) 5 mTorr, (b) 20 mTorr and (c) 80 mTorr.

**Figure 4.7.** FESEM cross-section view images of the films deposited by HiPIMS under (a) 0.7 Pa and (b) 0.9 Pa, respectively, with 0.5 kW and under (c) 0.7 Pa and (d) 0.9 Pa, respectively, with 0.7 kW.

**Figure 4.8.** FESEM top view images of the films deposited by HiPIMS under (a) 0.7 Pa and (b) 0.9 Pa, respectively, with 0.5 kW and under (c) 0.7 Pa and (d) 0.9 Pa, respectively, with 0.7 kW.

**Figure 4.9.** (a) growth rate, (b) resistivity and (c) roughness of the films deposited by HiPIMS

**Figure 4.10.** FESEM cross-section view images of the films deposited by HiPIMS with the substrate bias of (a) 0 V, (b) -10 V, (c) -20 V and (d) -30 V under the pressure of 0.7 Pa with the average power of 0.7 kW.

**Figure 4.11.** FESEM top view images of the films deposited by HiPIMS with the substrate bias of (a) 0 V, (b) -10 V, (c) -20 V and (d) -30 V under the pressure of 0.7 Pa with the average power of 0.7 kW.

**Figure 4.12.** (a) growth rate, (b) resistivity and (c) roughness of the films deposited by HiPIMS with the substrate bias under the pressure of 0.7 Pa with the average power of 0.7 kW.

**Figure 4.13.** Comparison of (a) growth rate and (b) resistivity of the films deposited by HiPIMS and RF magnetron sputtering.

**Figure 4.14.** Comparison of (a) XRD data and (b) FWHM of the films deposited by HiPIMS and RF magnetron sputtering.

## List of Tables

**Table 1.1.** Calculation of charge effect on the bond strength of Si–H and Si–Si in hydrogenated amorphous silicon [20].

**Table 2.1.** Characteristics of the Ti films with thickness, crystallinity, the calculated density and the measured critical angle by XRR at the electric bias of  $-70$  V,  $0$  V and  $+30$  V.

**Table 4.1.** Summary of results of HiPIMS.

# Table of Contents

## Chapter 1. Introduction

1.1. Non-classical crystallization .....	1
1.2. Chemical Vapor Deposition (CVD) .....	14
1.3. Physical Vapor deposition .....	18
1.3.1. Sputtering .....	19
1.3.2. Direct current (DC) sputtering .....	22
1.3.3. Radio frequency (RF) sputtering .....	23
1.3.4. High power impulse magnetron sputtering (HiPIMS) .....	25
1.4. Purpose of this study .....	27

## Chapter 2. Generation of charged Ti nanoparticles and their deposition behavior with substrate bias during RF magnetron sputtering

2.1. Introduction .....	33
2.2. Experimental method .....	36
2.3. Results and Discussion .....	38
2.4. Conclusion .....	43

## Chapter 3. Effect of pressure on the film deposition during RF magnetron sputtering considering charged nanoparticles

3.1. Introduction .....	53
3.2. Experimental method .....	56
3.3. Results and Discussion .....	58
3.4. Conclusion .....	66

## Chapter 3. Methods for growing low-resistivity tungsten film by controlling charged nanoparticles

4.1. Introduction .....	73
4.2. Experimental method .....	78
4.3. Results and Discussion .....	80
4.4. Conclusion .....	86

Bibliography .....	100
--------------------	-----

Abstract in Korean .....	110
--------------------------	-----

# **Chapter 1. Introduction**

## **1.1. Non-classical crystallization**

According to classical crystal growth mechanism, crystals should grow by the building blocks of individual atoms, ions and molecules. During chemical vapor deposition (CVD), thin films grow by atoms or molecules which are formed on the film surface or in the gas phase as a result of chemical reactions of precursors. According to terrace, ledge and kink (TLK) model, these atoms and molecules adsorb on a terrace and diffuse to a ledge, which are subsequently incorporated into the crystalline lattice of film at the kink [1, 2]. The atom adsorb on a terrace is called an adatom and has excess broken bonds, whereas the atom at the kink has no excess broken bond. Thus, during condensation and evaporation, reversible atom transfer only occurs at the kink.

However, there have been some phenomena that cannot be explained by the classical crystal growth mechanism. These

phenomena can be successfully explained by a new crystal growth mechanism in which thin films grow by building blocks of nanoparticles (NPs). This new concept of crystal growth is called ‘non-classical crystallization’ [3–7]. However, it is difficult to be accepted generally at first because the NPs have too small size to be detected, which are less than the wavelength range of visible light. Also, it is hard to be proved that the crystalline films and nanostructures are made by the NPs. However, recently in-situ transmission electron microscope (TEM) observation confirmed the non-classical crystallization and now it has become well established. Many books related to non-classical crystallization have been published and tutorial sessions of international conferences have been introduced.

The crystals that had been believed to be made by units of atoms, ions and molecules, now turn out to be made by building blocks of NPs. The non-classical crystallization has been extensively studied by Hwang et al. in the CVD process. They have published related text books and more than 80 SCI papers. [8–12] They emphasized that the charged carried by the NPs played a critical role in the deposition of thin films and nanostructures. [ref] This new crystal growth mechanism is called ‘theory of charged nanoparticles (TCN)’ . According to TCN, charged NPs which are spontaneously generated in the gas phase in most CVD processes



contribute to deposition of thin films and nanostructures. They suggested that neutral NPs undergo random Brownian coagulation and produce a porous structure. In contrast, charged NPs are self-assembled and undergo epitaxial recrystallization because the charge carried by the NPs weakens the bond strength of NPs. This makes the NPs liquid-like and consequently dense films or crystalline nanostructures are obtained.

TCN can well explain paradoxical phenomena in diamond deposition process. As shown in Figure 1.1, during diamond deposition process in CVD, very porous and graphitic soot particles grow on an iron substrate, whereas crystalline diamond films grow on a silicon substrate under the identical condition [7, 13]. These different deposition phenomena are related to the charge transfer rate of substrates. Diamond films are generated on the substrate having a low charge transfer rate whereas soot is generated on the substrate having a high charge transfer rate. According to Hwang et al., the charged diamond nuclei in the gas phase remain their diamond phase and charge when they approach the substrate having a low charge transfer rate. [9] Thus, these charged diamond nuclei undergo self-assembly because of their charge, like a colloidal of nanometer unit, and form crystalline diamond film as shown in Figure 1.1 (a). In contrast, when the charged diamond nuclei in the gas phase approach the substrate having a high charge transfer rate,

they lose their charge to the substrate and turn their structure into graphite. These neutral graphite nuclei undergo random Brownian coagulation and form very porous soot as shown in Figure 1.1 (b). It can be deduced that the charge carried by the diamond nuclei stabilize diamond structure. To confirm this deduction, Hwang et al. deposited films on floating and grounded iron substrates under the identical condition. Soot particles grew on grounded iron substrates, whereas diamond crystals grew on floating iron substrates. This could be explained that the charge carried by diamond nuclei in gas phase was reserved on the floating iron substrates and stabilize the diamond structure.

As mentioned above, Hwang et al. suggested that charged NPs are building blocks of thin films and nanostructures in most CVD processes. [9,10] The generation of these charged NPs in the gas phase was experimentally confirmed using a differential mobility analyzer (DMA) in many CVD systems [14–16]. Youn et al. used DMA to show the generation of charged silicon NPs in the gas phase during a silicon CVD process as shown in Figure 1.2. [17] Negatively and positively charged silicon NPs were generated in the gas phase and their size distribution was obtained using DMA. In addition, to show that these charged silicon NPs actually affect silicon film deposition, they compared the deposition behavior between floating and grounded silicon substrate. On the floating

substrate, the charge carried by the NPs would build-up whereas the charge would not build-up on the grounded substrate. Obvious differences between the two substrates are shown in Figure 1.3. The substrate temperature was 900° C and deposition time was 2 hours. Low- and high-magnification of field emission scanning electron microscopy (FESEM) images of the surface microstructure of film deposited on the floating substrate are shown in Figure 1.3 (a) and (b), respectively. As shown in Figure 3 (a) and (b), silicon nanowires with the diameter of 10 ~ 30 nm grew on the floating substrates. Figure 1.3 (c) and (d) are respectively low- and high-magnification of FESEM images of the surface microstructure of film deposited on the grounded substrates. On floating substrates, silicon nanowires were grown without catalytic metals or seeds of silicon oxide. Vapor-liquid-solid (VLS) [18] and oxide-assisted growth (OAG) mechanism [19] cannot explain this deposition. The only difference between the two experiments is the substrates, which means that the charge build-up on the substrates would be the reason of these different deposition behavior. The reason that nanowires grew on the floating substrates is that self-assembly of NPs occurred because of the charged carried by the NPs. In addition, although the nanowire grew by building blocks of NPs, the reason that the NPs grew into ‘rod-shaped single crystal’ rather than in the form of a pearl necklace-shape is also that diffusion was promoted by the charge.

When the flow rate of carrier gas increased, films were grown on both floating and grounded substrates as shown in Figure 1.4. Figure 1.4 (a) and (b) shows top view and cross-section view of FESEM images of the films deposited on floating substrates, respectively. Also, Figure 1.4 (c) and (d) shows top view and cross-section view of FESEM images of the films deposited on grounded substrates, respectively. As described earlier, obvious deposition difference was shown between the two substrates. In Figure 1.4 (a) and (b), a dense film of 220 nm thickness was deposited on the floating substrate. This is thought to be due to the electrostatic interaction between charged NPs and the growing surface. On the other hand, looking at Figure 1.4 (c) and (d), a 190nm-thick porous film was deposited on the grounded substrate. This is also believed to be due to the fact that there was little electrostatic interaction in the growing surface. Therefore, the amount deposited on a floating substrate is much higher than that of a grounded substrate. That is, as the charge build-up differs on a floating substrate and a grounded substrate, the deposition behavior of charged silicon NPs is very different. This study shows that charge plays a very important role to obtain smooth nanowire or dense film.

From the research results described so far, it can be seen that charged NPs are liquid-like, that is, charge weakens the bond

strength of NPs. To confirm this possibility, we searched the results of related studies. Clare et al studied the effect of charge on the bond strength of hydrogenated amorphous silicon. [20] The effect of a single negative or positive charge on the strength of Si-Si and Si-H bonds in the  $\text{SiH}_4$  and  $\text{Si}_2\text{H}_2$  molecules was calculated by ab initio calculations. To find out the difference in energy required to break a single Si-H bond in  $\text{SiH}_4$ ,  $\text{SiH}_4^+$  and  $\text{SiH}_4^-$  were calculated for the following 6 types:  $\text{SiH}_3$ ,  $\text{SiH}_3^+$ ,  $\text{SiH}_3^-$  and  $\text{SiH}_4$ ,  $\text{SiH}_4^+$ ,  $\text{SiH}_4^-$ . Also, the required energy was determined by comparing the bond strength of each species. In addition, to find the effect of a lower charge/size ratio and to determine the effect of charge on the Si-Si bond energy, this calculation was done for  $\text{Si}_2\text{H}_6$ ,  $\text{Si}_2\text{H}_6^+$ ,  $\text{Si}_2\text{H}_6^-$ ,  $\text{Si}_2\text{H}_5$ ,  $\text{Si}_2\text{H}_5^+$  and  $\text{Si}_2\text{H}_5^-$ . The results of the calculations are summarized in Table 1.1. If atoms are lodged in a lattice, they cannot achieve a shape similar to the optimized ionic shape, although they can relax to some extent. So, in hydrogenated amorphous silicon, the actual effect of charge on bond strength will be between what is represented by the unoptimized (adiabatic) row and the optimized (vertical) row in Table 1.1. It will be closer in case of unoptimized rows. Both positive and negative charges significantly weaken the bonding strength of Si-Si and Si-H. The bonding strength of Si-Si weakens from 3.2 eV to 1.11 eV when  $\text{Si}_2\text{H}_6$  is negatively charged. When  $\text{Si}_2\text{H}_6$  is positively charged, it weakens to 1.6 eV. The bonding strength of Si-H is significantly

weakened from 3.9 eV to 0.98 eV when SiH<sub>4</sub> is negatively charged. When SiH<sub>4</sub> is positively charged, it weakens to 0.3 eV. The effect of charge on bond strength can be explained by the bond order of molecular orbital theory. The bond order, which indicates the strength or stability of a bond, is the number of bond electron pairs shared by two atoms in a molecule. The order of bonding is defined as half the difference between the number of bonded and prevented electrons expressed by the following equation (1.1)

$$\text{Bond order} = \frac{\text{\#of bonding electrons} - \text{\#of antibonding electrons}}{2} \quad (1.1)$$

If NPs are negatively charged, electrons are added to the anti-bonding orbitals. When NPs are positively charged, electrons are removed from the bond orbitals. So, both positive and negative charges reduce bond orders, weakening bond strength. The weakening of the bond strength caused by electric charges is of great importance because it means improved diffusion or dynamics. As a result, the weakening of the bond strength by charge can explain the liquid-like properties of charged NPs. Thus, these experimental and computational results can explain the rapid kinetics of coalescence by the charge, where the chemical reaction of the reactant gases is enhanced even at low temperatures and crystalline films are deposited at low temperatures in most CVD and some PVD processes.

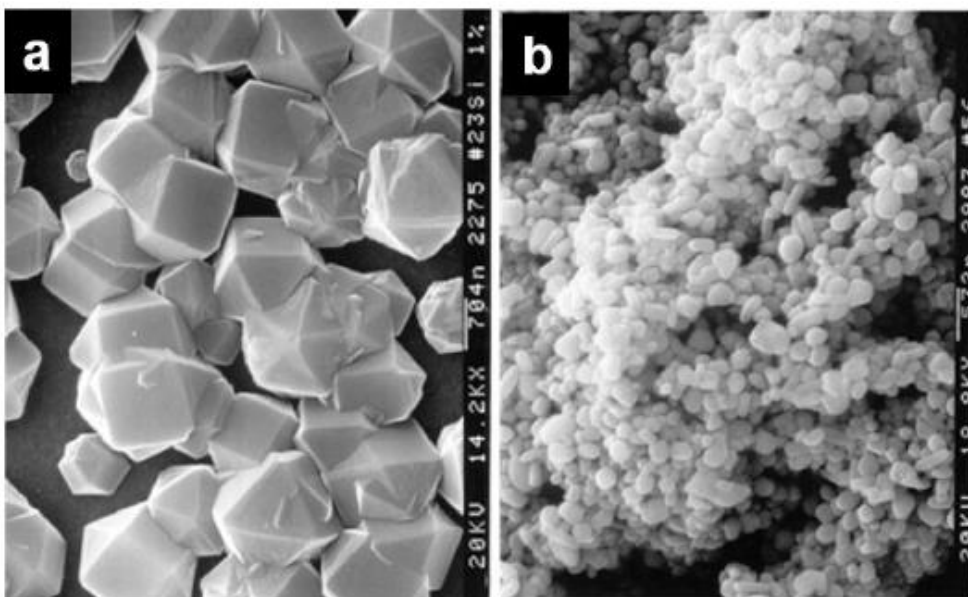


**Figure 1.1.** (a) Diamond and (b) soot grown on Si and Fe substrates, respectively [7, 13].

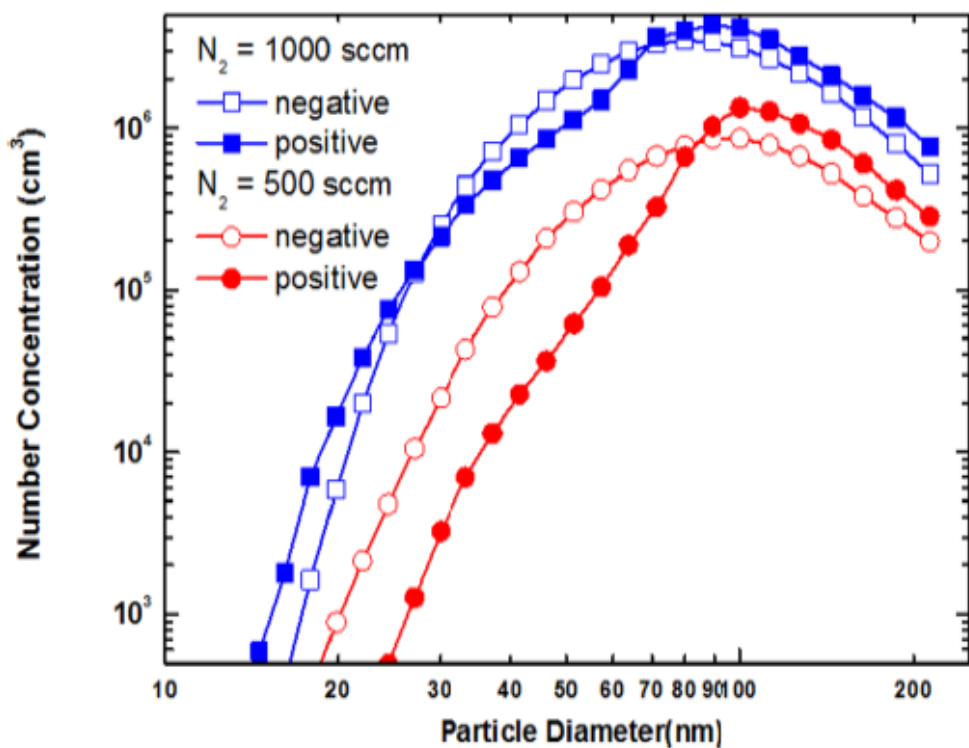
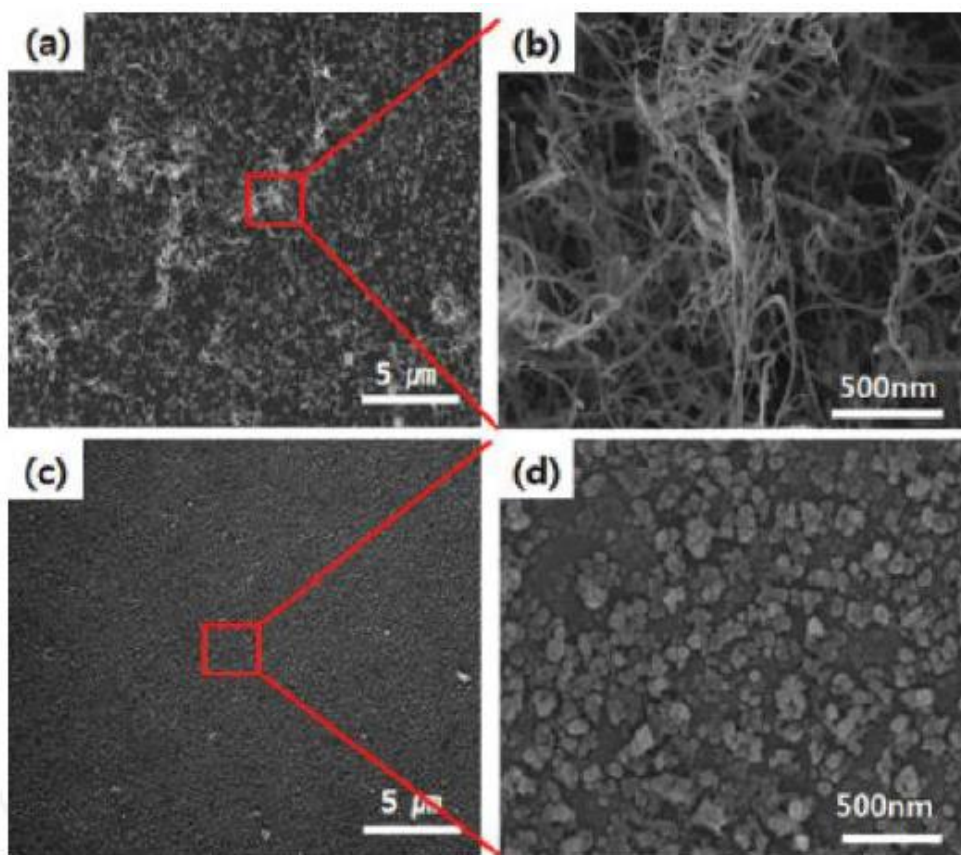
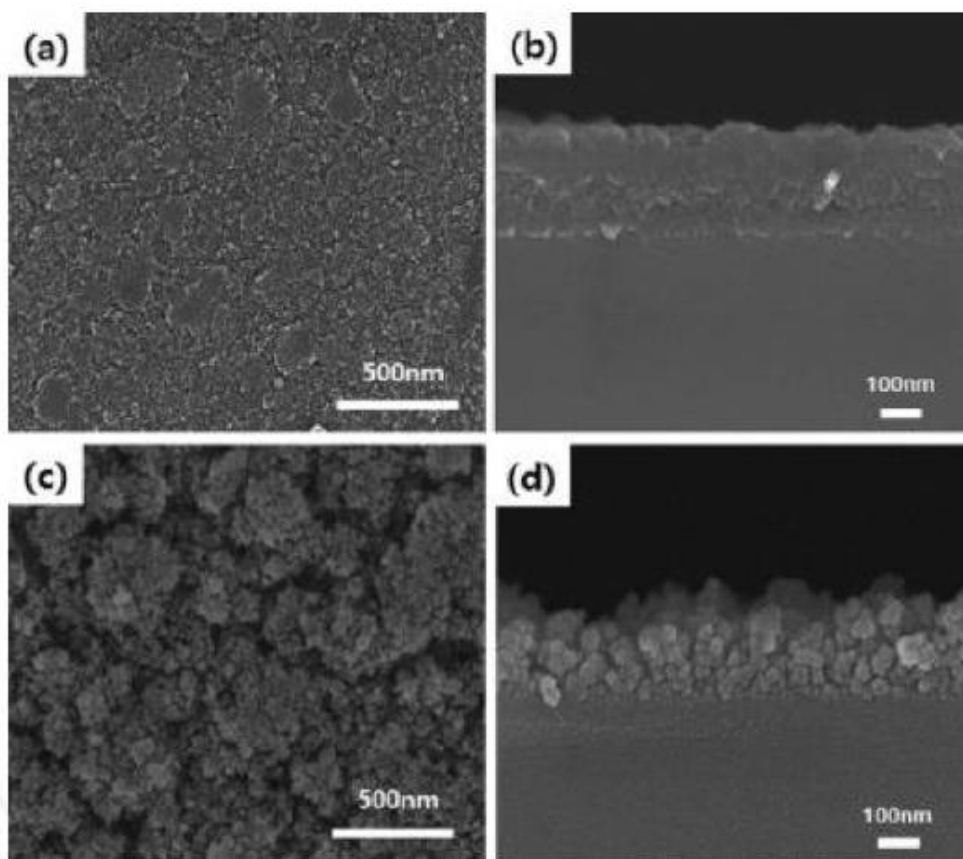


Figure 1.2. Number concentrations and size distributions of negatively (open) and positively (closed) charged NPs at a N<sub>2</sub> flow rate of 500 sccm and 1000 sccm, respectively [17].





**Figure 1.3.** FESEM images of (a) low and (b) high magnification images of a floating substrate and (c) low and (d) high magnification images of a grounded substrate with a  $N_2$  flow rate of 500 sccm [17].



**Figure 1.4.** FESEM images of (a) top and (b) cross-section view images of a floating substrate and (c) top and (d) cross-section view images of a grounded substrate with a  $N_2$  flow rate of 1000 sccm [17].

**TABLE X.**  
**Summary of Si—H and Si—Si Bond Strengths.**

Compound	Si—H (eV)	Si—Si (eV)
SiH <sub>4</sub> (optimized)	3.9	—
SiH <sub>4</sub> <sup>−</sup> (optimized)	0.98	—
SiH <sub>4</sub> <sup>+</sup> (optimized)	0.30	—
Si <sub>2</sub> H <sub>6</sub> (optimized)	3.5	3.2
Si <sub>2</sub> H <sub>6</sub> <sup>−</sup> (optimized)	1.02	1.11
Si <sub>2</sub> H <sub>6</sub> <sup>+</sup> (optimized)	1.59	1.6
SiH <sub>4</sub> <sup>−</sup> (unoptimized)	1.35	—
SiH <sub>4</sub> <sup>+</sup> (unoptimized)	0.09	—
Si <sub>2</sub> H <sub>6</sub> <sup>−</sup> (unoptimized)	1.34	1.3
Si <sub>2</sub> H <sub>6</sub> <sup>+</sup> (unoptimized)	1.49	1.6

Table 1.1. Calculation of charge effect on the bond strength of Si—H and Si—Si in hydrogenated amorphous silicon [20].

## **1.2. Chemical vapor deposition (CVD)**

In the chemical vapor deposition (CVD) method, when a gaseous source gas containing a desired material is injected into a reactor, energy is received from heat or plasma and decomposed. At this time, the desired material reaches the substrate to form a film. CVD is largely composed of a gas distribution device, a reactor, and a pump device. CVD is classified in various ways according to the pressure of the reactor, the energy source of the chemical reaction, the temperature of the reactor wall, the reaction temperature, the shape of the reactor, and the reaction raw material. In a normal CVD process, a room temperature reactant is introduced into the reaction chamber. This gas mixture is heated up to the evaporation surface and is continuously supplied with heat by convection or heating of the evaporation surface. Depending on the various process conditions, the reactant gas may cause a homogeneous reaction in the gas phase before reaching the deposition surface. Near the deposition surface, the gas flow is heated, the velocity decreases due to viscosity, and the composition changes. A boundary layer of composition is formed. The introduction gas or reaction intermediate causes a heterogeneous reaction on the deposition surface, thereby forming a thin film. Subsequently, gaseous by-products exit the reaction chamber.

CVD runs in a variety of formats. These processes usually differ in the means by which chemical reactions are initiated. First, CVD is classified according to its operating conditions. Atmospheric pressure CVD (APCVD) operating at atmospheric pressure (APCVD), low pressure CVD (LPCVD) operating below atmospheric pressure. [21] Low pressure tends to reduce unwanted gas phase reactions and improve film uniformity across the wafer. Ultra-high vacuum CVD (UHVCVD) operating at very low pressures, typically less than  $10^{-8}$  torr. In other applications, a low distinction between high and ultra-high vacuum is common.  $10^{-9}$  torr. The most modern CVD is LPCVD or UHVCVD.

Additionally, CVD is classified by the physical properties of the vapor. Aerosol-assisted CVD (AACVD) in which precursors are transported to a substrate through a liquid/gas aerosol that can be generated by ultrasonic waves. This technique is suitable for use with non-volatile precursors. And it determines liquid injection CVD (DLICVD) in which the precursor is in liquid form (liquid or solid dissolved in a convenient solvent). The liquid solution is injected from the vaporization chamber towards the injector (typically a car injector). The precursor vapor is then transferred to the substrate as in conventional CVD. This technique is suitable for use with liquid or solid precursors. High growth rates can be reached with this technique.

In addition, CVD is classified according to the type of substrate heating. The chamber's hot wall CVD is heated by an external power source and the substrate is heated by radiation from the heated chamber wall. And low-temperature wall CVD where only the substrate is directly heated by induction or by passing an electric current through the substrate itself or a heater in contact with the substrate. The chamber walls are room temperature.

At last, there are types of CVD that the plasma method supports. Plasma Enhanced CVD (PECVD) uses plasma to speed up the chemical reaction of precursors. [22] The PECVD process enables deposition at low temperatures, which are often critical in semiconductor manufacturing. Low temperatures can also remove the location of organic coatings such as plasma polymers used for nanoparticle surface functionalization. [23] And remote plasma enhanced CVD (RPECVD) is similar to PECVD except that the wafer substrate is not directly in the plasma discharge area. Processing is possible by removing the wafer from the plasma area. It goes down to room temperature. LEPECVD (Low Energy Plasma Enhanced Chemical Vapor Deposition) uses a high density, low energy plasma to obtain epitaxial deposition of semiconductor materials at high speed and low temperature. Atomic layer CVD (ALCVD) deposition. Successive layers of different materials produce a layered crystalline film. Combustion chemical vapor

deposition (CCVD) is an open atmosphere, flame-based technology for depositing high-quality thin films and nanomaterials. Hot filament CVD (HFCVD), also known as catalytic CVD (Cat-CVD) or more commonly initiated CVD (iCVD), uses hot filaments to chemically break down the source gas. [24] Thus, the filament temperature and substrate temperature are controlled independently, allowing a lower temperature for better absorption at the substrate and higher temperatures required to decompose the precursor from the filament to free radicals. [25] Hybrid Physical Chemical Vapor Deposition (HPCVD) involves both chemical decomposition of precursor gases and evaporation of solid sources. Metal organic chemical vapor deposition (MOCVD) is based on metal organic precursors. Rapid Thermal CVD (RTCVD) rapidly heats a wafer substrate using a heating lamp or other method. Heating only the substrate, not the gas or chamber walls, helps reduce unwanted gas phase reactions that can lead to particle formation. Photo Initiated CVD (PICVD) uses UV light to stimulate chemical reactions. It is similar to plasma treatment, given that the plasma emits strong UV radiation. Under certain conditions, PICVD can operate at or near atmospheric pressure. [26] Laser chemical vapor deposition (LCVD) uses a laser to heat a spot or line.

### **1.3. Physical vapor deposition (PVD)**

PVD is a vacuum deposition method that can be used to deposit or coat thin films. PVD has a process of converting a source material, which exists as a condensation step, into a vapor step, and then converting it into a thin film-shaped condensation step. The most common PVD processes are sputtering and evaporation. PVD is used in the manufacture of items that require thin films with various mechanical, optical, and electrical properties. [27–29] In this process, the source material is deposited not only on the thin film, but also on most other surfaces inside the vacuum chamber.

PVD can obtain a harder and corrosion-resistant thin film compared to the electroplating process. And most of them are stable at high temperatures, have excellent impact strength and abrasion resistance, and therefore do not require a protective coat. In addition, virtually any type of inorganic and some organic coating can be applied to a variety of substrates and surfaces.

In contrast, as a disadvantage, since most of PVD is deposited on the line of sight, it is difficult to coat complex shapes. And since some PVD processes generally require very high temperatures or very high vacuum levels, they are not easy to maintain. In addition,



a cooling system is required to stably use high temperatures.

### **1.3.1. Sputtering**

Sputtering deposition is one of the PVD processes using sputtering of a target material. [30] That is, particles generated by sputtering a target used as a source reach a substrate such as a silicon wafer, and a thin film is deposited. In Figure 1.5, when the ions hit the target surface, this sputtering occurs. Ions can be reflected and neutralized immediately. This scattering process is the basis of an analytical technique called ion scattering spectroscopy. Ion bombardment can release electrons from the target, and these electrons are called secondary electrons. Ions can penetrate the target. This process, known as ion implantation, is widely used in integrated circuit technology to dope silicon wafers selectively. It can control the depth and amount of impurity atom atoms. Ions can cause structural changes in the target material. These changes can lead to changes in target composition due to major lattice defects as well as simple vacancies and interstitial defects.

Ion bombardment can cause a series of collisions between

target atoms. This ejection process is called sputtering. This continuous current glow discharge, which generates energetic particles that support the sputtering process, can be obtained by applying a potential difference between the two electrodes with sputtering gas maintained at low pressure inside the vacuum chamber. The abbreviated process is shown in Figure 1.6. Voltage can be delivered by a power supply that provides tens of thousands of volts of energy. As a result, an electric field is generated between the two electrodes. This electric field accelerates electrons or ions formed by thermionic emission or collisions or reaction with cosmic rays. Sequentially these accelerated electrons collide with other atoms or ions and generate more electrons, which generate discharge between the electrodes.

The sputtered atoms emitted from the target typically have a wide energy distribution, up to tens of eV. The sputtered ions fly straight away from the target and energetically impact the substrate or vacuum chamber, which is called re-sputtering. Alternatively, at higher gas pressures, ions act as mediators and collide with diffusely moving gas atoms, reacting back to the substrate or vacuum chamber wall, and condensate after going through a random walk. By changing the background gas pressure, it is accessible to the full range from high energy ballistic impacts to low energy aging motions. Sputtering gas is often an inert gas such as argon. For

efficient momentum transfer, the atomic weight of the sputtering gas must be close to that of the target. Therefore, for sputtering, light elemental neon is preferred, and for heavy elements, krypton or xenon is used. Compounds can also be sputtered using reactive gases. The compound can form on the target surface, in flight, or on the substrate depending on the process parameters. Not only is it a complex process because there are so many parameters available to control sputter deposition, but it also gives professionals great control over the growth and microstructure of the film.

One of advantages of sputter deposition is that even very high melting point materials are easily sputtered, whereas evaporating these materials is very hard or impossible. The film deposited by sputtering has a composition similar to that of the source material. If they are different, it is because the elements are spread out differently because of different masses. The films deposited by sputtering generally show better adhesion to the substrate than the films deposited by evaporation. Other advantages of sputter deposition is that the target contains large amounts of material and requires no maintenance, making it a suitable technology for ultra-high vacuum applications. The sputtering source does not contain hot components and is compatible with reactive gases such as oxygen. Sputtering can be done top-down, and evaporating ions should be done bottom-up. It is also possible to use advanced

processes such as epitaxial growth.

One of drawbacks of the sputtering process is that it is more difficult to combine the process with lift-off for film structuring due to diffuse transmission, which is a characteristic of sputtering. This makes the entire shadow impossible. Thus, it is impossible to limit where the atoms go, which can cause contamination problems. In addition, active control for layer-by-layer growth is difficult compared to pulsed laser deposition, and inert sputtering gas can be embedded as impurities.

### **1.3.2. Direct current (DC) sputtering**

DC sputtering system consists of a pair of planar electrodes as described in section 1.3.1. As can be seen in Figure 1.7, one of the electrodes, which is a cathode, is the target and the other electrode, which is an anode and where the substrate is mounted, is grounded. The opposite side of the cathode is cooled by water. Argon gas is injected to maintain the pressure of chamber and to maintain plasma between electrodes. A voltage of several kilovolts is applied between the electrodes to initiate the glow discharge. The positive argon ions present in the plasma are accelerated toward the cathode,

which cause sputtering of the target atom. The sputtered atoms diffuse and reach the substrate, resulting to deposit a thin film. The cathode of a DC diode system, which is a target, must be conductive. If the target is an insulator, charge will build up on the target surface and ion bombardment on the target surface will be prevented.

By introducing a suitable magnet behind the target, the electrons in the plasma can be kept close to the target surface. Thus, the electron density can be increased by the magnetic field. This system is called DC ‘magnetron’ sputtering and shown in Figure 1.8. High density plasma can be obtained by this high electron density and this makes more ions to bombard the target. This electron trapping by the magnetic field increases the probability of ionization of neutral molecules in the gas by several times. Also, this increasing ion density greatly improves the sputter yield and the deposition rate of the substrate, which make sputtering at low pressure possible.

### **1.3.3. Radio frequency (RF) sputtering**

When the target is an insulator, the glow discharge does not last,

because charge will build up immediately on the insulating target surface. To maintain a glow discharge with an insulating target, the DC power supply must be replaced by an RF power supply, which is called RF sputtering system. When an RF potential is connected to an electrode, the electrode turns to the anode and cathode alternately. During each half of a cycle applying negative potential to the target, ions are accelerated towards the target surface and can have enough energy to sputter. During the other half of a cycle, positive potential is applied to the target and electrons are accelerated towards the target surface. These electrons neutralize the positive charge build up and prevent the formation of a charge barrier. This system requires an impedance matching network between the power supply and the chamber. The impedance of the RF source is typically 50 ohm and the discharge impedance is within range of 1 to 10 k-ohm. In this system, the current density is given by the following equation.

$$I_s \cong C dV/ dt$$

where C is the capacitance between the plasma and the target and dV/dt is the change of the target surface potential over time. From this equation, it can be observed that the ion current at the cathode increases with increasing frequency. The frequency applied in commercial systems is 13.56 MHz.

As described, since RF sputtering 'cleans' the target surface in each cycle, there is less risk of arc generation. Arcing occurs when a localized and concentrated discharge occurs in the electrode, which is released into the plasma. Since RF sputtering reduces charge build-up on the target surface, arcing generation can be reduced, and numerous quality control problems can be reduced.

Also, RF sputtering reduces the generation of 'track erosion' on the target surface. Electrons are trapped around the target by the magnetron as described above, and the trapped electrons sputter the target in the magnetic field direction. That is, erosion occurs in the magnetic direction on the target surface, and in the case of RF sputtering, the generation of this erosion can be reduced. In rf sputtering, since electrons are less trapped in the magnetic field compared to dc sputtering, the width and depth of this erosion is much smaller.

### **1.3.4. High power impulse magnetron sputtering**

HiPIMS is a relatively recently developed magnetron sputtering process. HiPIMS creates a high density plasma and increases the ionization rate by applying a very high voltage for a short duration.

A high voltage in the unit of  $\text{kW cm}^{-2}$  is applied to the target in a pulse method, but since it has a short duty time within 10%, it does not overheat the target or other process systems. Targets heated during the duty time are cooled during off duty, and as a result the average power is low enough to keep the system stable.

The high voltage and resulting high ionization rate of HiPIMS improve film adhesion and uniformity. Also, HiPIMS makes it possible to deposit more uniform film on complex shaped substrates. Because of these advantages, HiPIMS becomes popular for tough and dense film with less void where conventional deposition processes do not deposit uniform film on irregular shaped substrates.

These characteristics of HiPIMS are enabled by the pulsing. Pulsing creates ionized atoms at much higher energy levels than conventional sputtering. Also, this significantly increases the probability of ionizing collisions and the sputtered material ionizes and collides with the process gas atoms. Thus, HiPIMS generates high plasma density of  $10^{13} \text{ ions cm}^{-3}$  that is much higher than conventional sputtering processes. Another advantage of HiPIMS is that it is very simple to install. Conventional sputtering system can be retooled into HiPIMS system just introducing suitable power supply for HiPIMS.



One of the drawbacks of HiPIMS is arcing. Because of high voltage of HiPIMS, there can be heavy arcing spreading from the cathode to plasma. This can overheat the target or even make droplets from the target that can cause problem to film deposition.

## **1.4 Purpose of this study**

Theory of charged NPs has been confirmed by many experiments and calculations. The generation of NPs was confirmed during many CVD systems and their polarity of charge was also verified. Theory of charged NPs has been applied to larger area and become so established that many regarding books and papers have been published.

However, the area of theory of charged NPs has been rather limited to CVD system. It is well applied to CVD system and now it is necessary to confirm the theory to PVD system. A few PVD system like evaporation has been studied and the theory also can be applied to evaporation system. Thus, the generation of charged NPs is expected during other PVD system and the regarding study is needed. Especially sputtering is a very widely used deposition process of PVD. Also, sputtering process uses plasma, which consists of many charged species like ions and electrons. Thus, the

generation of charged NPs during sputtering is well expected and needs to be studied.

Therefore, the main purpose of this Ph. D course is to confirm the generation of charged NPs during sputtering, especially RF magnetron sputtering and to investigate how these charged NPs affects the actual film deposition. After confirming the generation of charged NPs, it was investigated how the behavior of these charged NPs and their effect on film deposition depend on pressure.

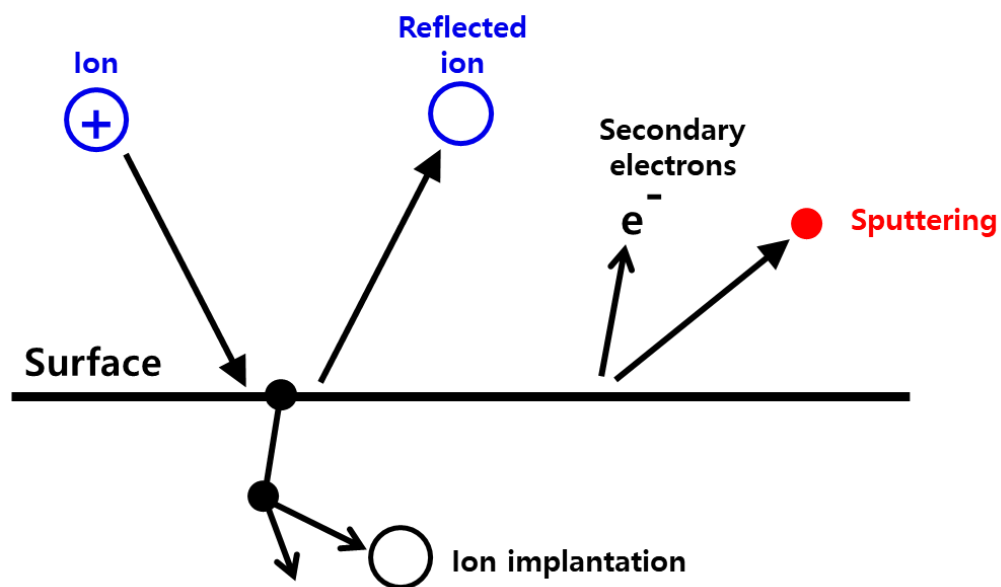
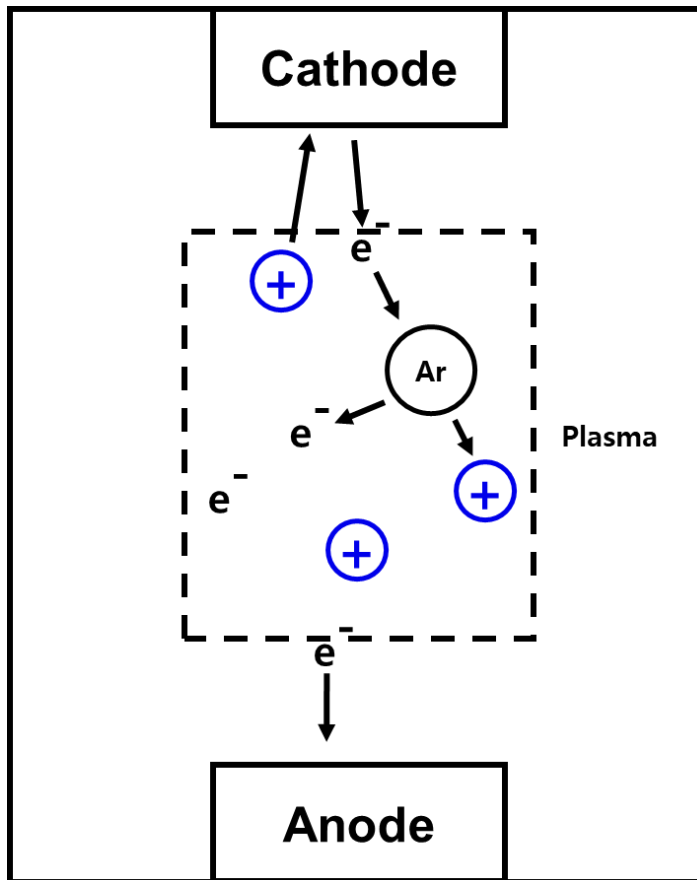


Figure 1.6. Phenomena on the target surface by ion bombardment



**Figure 1.7.** Glow discharge formation inside the vacuum chamber for generating the energetic particles.

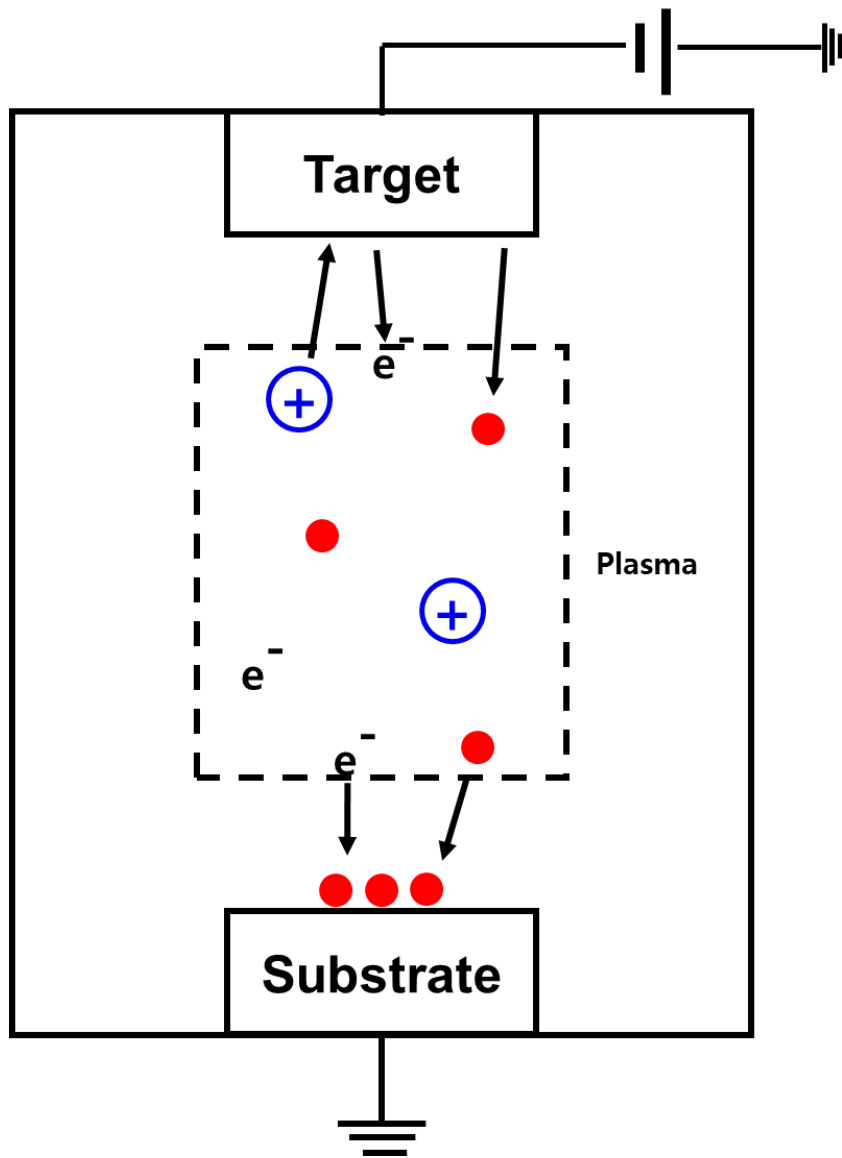
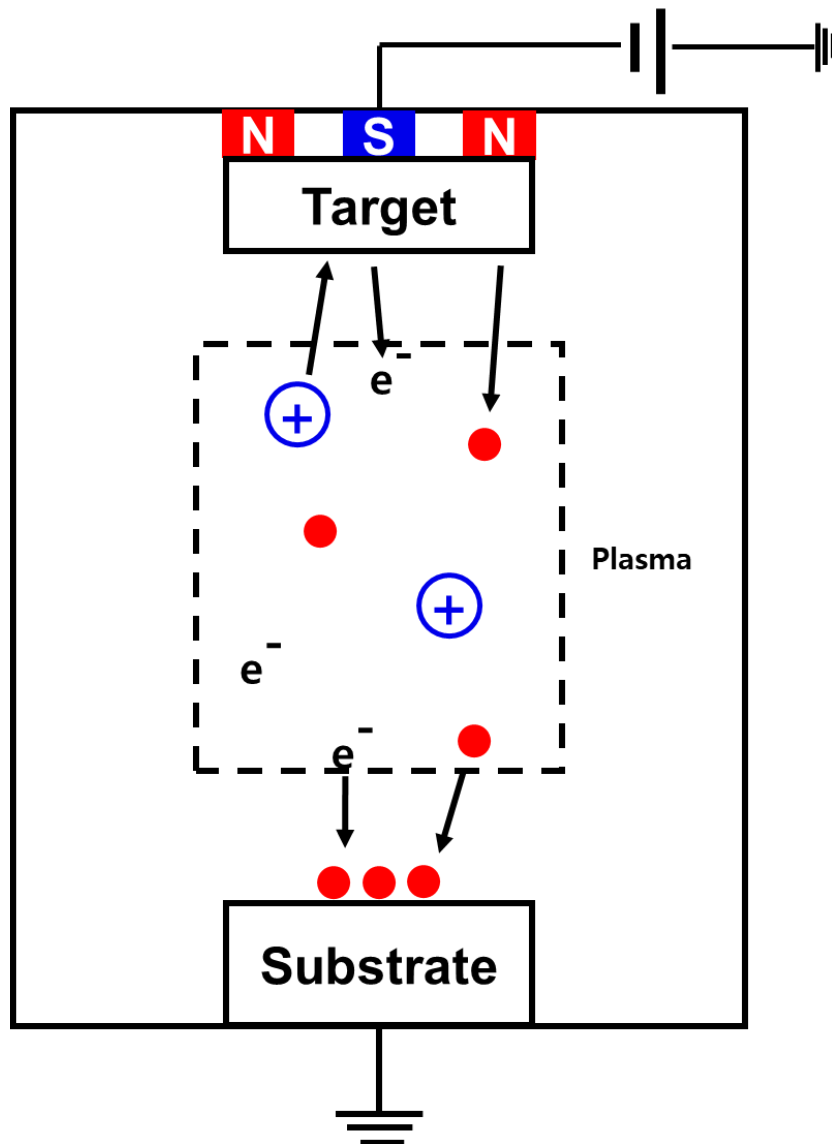


Figure 1.8. Schematics of a conventional DC sputtering system.



**Figure 1.9.** Schematics of a conventional DC magnetron sputtering system.

# **Chapter 2.**

## **Generation of charged Ti nanoparticles and their deposition behavior with substrate bias during RF magnetron sputtering**

### **2.1. Introduction**

Titanium (Ti) thin films have outstanding properties such as good biocompatibility, good thermal and chemical stability [31–36]. Thus, Ti thin films are widely used in biomedical applications and microelectronics. Ti films are mainly obtained by direct current (DC) sputtering or radio frequency (RF) sputtering, which are well established technology in the industry to deposit thin films because of their high reproducibility and growth rates [37–43].

On the other hand, according to classical crystallization, it has

been believed that thin films are deposited by individual atoms, ions or molecules. However, there are several phenomena that cannot be explained by classical crystallization. These phenomena can be successfully explained by a novel growth mechanism where thin films are deposited by building blocks of nanoparticles (NPs). This growth mechanism has been supported by a lot of experimental evidence and is called 'non-classical crystallization' [44–50].

According to Hwang et al. who have extensively studied non-classical crystallization in CVD system, it is suggested that the electrically charged NPs are spontaneously generated in the gas phase during CVD system and become the building blocks of thin film [51]. Also, the charge carried by the NPs critically affects deposition of crystalline thin films and synthesis of crystalline nanostructures such as nanorod and tetrapod [52–57]. This new crystal growth mechanism is called 'theory of charged NPs (TCN)' . According to TCN, neutral NPs undergo random Brownian coagulation resulting in porous structure. In contrast, charged NPs produce ordered structure by self-assembly. Because these charged NPs have liquid-like property, they undergo epitaxial recrystallization after self-assembly, resulting in dense and crystalline structures. The liquid-like property can be explained by the calculation that the charge can weaken the bond strength. Indeed, Clare et al. conducted the *ab-initio* calculation and reported



that the bond strength of Si–H and Si–Si is weakened by the charge in  $\text{SiH}_4$  and  $\text{Si}_2\text{H}_6$  molecules [20]. In addition, many experiments in CVD system supports these understandings of TCN. For instance, homoepitaxial Si films were deposited on negatively biased Si substrates at low substrate temperature of  $550^\circ\text{C}$  during plasma enhanced CVD [58]. Crystalline and dense Si films were deposited by controlling the behavior of Si charged NPs during inductively coupled plasma CVD [59].

A few researches have been studied to utilize NPs for thin film deposition in PVD system. Sahu et al. modified magnetron into 3–D confined magnetron to induce the generation of crystalline NPs and enhanced the property of indium tin oxide films [60]. Hayasaki et al. also deposited epitaxial yttrium barium copper oxide films by inducing nano–sized clustering during thermal plasma flash evaporation [61]. However, these researches did not concern the charge carried by NPs carefully.

Thus, in this paper, the generation of NPs and the charge of NPs were carefully investigated during conventional RF sputtering system using Ti target. Also, effect of charged NPs on film deposition was confirmed. The generation of NPs and their polarity were confirmed by capturing them on amorphous carbon membranes with applying electric bias. Amorphous carbon

membranes were analyzed by transmission electron microscopy (TEM). The effect of charged NPs on film deposition was investigated by the electric bias on substrates. Property of films was analyzed by TEM, field-emission scanning electron microscopy (FESEM) and x-ray reflectivity (XRR).

## **2.2. Experimental method**

Figure 2.1a shows schematics of RF sputtering system with Ti target. The distance between the Ti target and a sample stage was 7 cm. Amorphous carbon TEM membrane (Ted Pella, Inc.) was used as substrate for capturing NPs and a p-type Si substrate was used as substrate for film deposition. Substrates were placed on a steel plate. In order to apply electric bias on the steel plate, the steel plate was electrically isolated with the grounded sample stage. Also, to prevent the electric bias of the steel plate from interfering with plasma, a grounded mesh in Figure 2.1b was installed 2 mm above the steel plate. Electric field will be generated between the grounded mesh and steel plate. If charged NPs exist, they would interact with the electric field.

To control the exposure time for capturing NPs or film

deposition, a round-shaped shutter with diameter of 5 cm was installed 5 mm above the grounded mesh. This means that the flux from plasma was blocked when the shutter was closed. When the shutter was opened, and the capture or film deposition started.

Ar gas was used to sustain plasma and pressure was 20 mTorr. RF sputtering power was 160 W and the heating system for substrate temperature was not used. NPs were captured on amorphous carbon TEM membrane for 30 sec. To confirm the charge of NPs, various electric bias of -70, 0, +5, +15 and +30 V was applied to the membrane. Also, to investigate the effect of Ti charged NPs on the film deposition, Ti films were deposited under the same condition with capturing NPs on p-type (100) Si substrates for 30 min with the substrate bias of -70, 0 and +30 V.

To stabilize plasma, the capturing NPs and film deposition processes were conducted 30 sec after turning on the plasma. Any flux from plasma to TEM membrane or Si substrate were perfectly blocked by the shutter during stabilizing.

The NPs were analyzed by TEM (FEI, Tecnai F20). The microstructure of Ti films was analyzed by SEM and TEM. The density of the films was calculated by measuring critical angles of XRR.

## 2.3. Results and discussion

### 2.3.1. Capturing charged NPs during RF sputtering with Ti target

The electric field generated between the grounded mesh and the steel plate will interact with charged NPs. White dots are shown in scanning transmission electron microscope (STEM) images in Figure 2.2. These dots are confirmed to be titanium dioxide ( $\text{TiO}_2$ ) NPs by the fast Fourier transformation as shown in inset of Figure 2.3. NPs were captured with applying various steel plate bias of  $-70$ ,  $0$ ,  $+5$ ,  $+15$  and  $+30$  V. As shown in Figure 2, the number density of NPs increased as increasing negative bias from  $0$  V to  $-70$  V. In contrast, it decreased as increasing positive bias from  $0$  V to  $+30$  V. From these results, the NPs are thought to be positively charged. Thus, it is thought that they were attracted to the TEM membrane when negative bias was applied to membrane, whereas they were repelled when positive bias was applied. As the positive bias get bigger, the more positively charged NPs would be repelled according to energy distribution of NPs.

The result at  $+30$  V should be focused. There was no NPs that was observed on the TEM membrane at  $+30$  V as shown in Figure 2.2 (e). This might be attributed to that all positively charged NPs

were repelled by +30 V, which means that there was no NPs that was more energetic than +30 V. On the other hand, in case of negatively charged NPs, they were expected to be blocked by potential difference between plasma and the grounded mesh. Because the grounded mesh had more negative potential with respect to plasma, there was negative potential difference between the grounded mesh and plasma. Thus, it is thought that there was no negatively charged particle that was energetic enough to overcome the negative potential difference.

Neutral NPs should land on the TEM membrane regardless of the sign of bias. However, there was no NPs observed on TEM membrane at +30 V. Thus, there are two possibilities to explain the absence of neutral NPs on the TEM membrane at +30 V. One possibility is that neutral NPs did not exist, so that they were not observed. The other possibility is that the neutral NPs had too small size that they could not be observed by HRTEM although they landed on the TEM membrane. To check these possibilities, Ti thin films were deposited under the same conditions with capturing the charged NPs. This will be discussed in chapter 2.3.2.

As discussed above, the white dots in Figure 2.2 were confirmed to be  $\text{TiO}_2$  by FFT analysis. The insets of Figure 2.3 show fast Fourier transformation of HRTEM images, which are the

NPs captured at  $-70$  V and  $0$  V. The captured NPs had the average size of  $\sim 5$  nm and d-spacing of  $\sim 0.217$  nm mainly, which corresponded to the value of  $\text{TiO}_2$ . This is due to the oxidation of Ti NPs immediately after they were taken out of the vacuum chamber and exposed to air, because Ti becomes oxidized very easily [62].

### 2.3.2. Ti thin film deposition

As mentioned in earlier chapter 2.3.1, Ti films were deposited under the same conditions with capturing the charged NPs on Si (100) substrates for 30 min. The films were deposited with applying bias of  $-70$ ,  $0$  and  $+30$  V. Figure 2.4 shows the cross-section view SEM images of these films. Thickness of the films deposited at  $-70$ ,  $0$  and  $+30$  V was respectively 180, 146 and 92 nm. Compared to the film at  $0$  V, thickness of the films increased when applying negative bias of  $-70$  V, whereas it decreased when applying positive bias of  $+30$  V. This should be due to attraction and repelling of positively charged NPs by the substrate bias.

Although there was no NPs observed in case of  $+30$  V as discussed earlier, film was deposited at  $+30$  V as shown in Figure 2.4c. If neutral NPs did not exist indeed, the film would be deposited by only neutral atoms like atomic layer deposition. It means that the film should have the highest crystallinity and density

among all films deposited at  $-70$ ,  $0$  and  $+30$  V. As the second possibility, if neutral NPs had too small size that they could not be observed by HRTEM although they landed on the TEM membrane as discussed above, the film would be deposited also by the minute-sized neutral NPs not only by atoms. It means that the film should have very low crystallinity and density or even porous structure. In this regard, Jeon et al. reported that the film deposited by high fraction of neutral clusters showed rough surface morphology and fractal structure whereas the film with high fraction of charged clusters showed smooth morphology and high quality during copper thermal evaporation [52]. Thus, to confirm these two possibilities, property of the films deposited at  $-70$ ,  $0$  and  $+30$  V was analyzed. Crystallinity and density of the films were analyzed.

Figure 2.5a–c show low magnification HRTEM images of the films at  $-70$ ,  $0$  and  $+30$  V, respectively. Also, Figure 2.5d–f show high magnification HRTEM images of the films at  $-70$ ,  $0$  and  $+30$  V, respectively. As shown in Figure 2.5d–f, the films at  $-70$  and  $0$  V show obvious lattice fringe images and FFT images. However, the film at  $+30$  V show obscure images. Amorphous regions of the films at  $+30$  V are marked by ovals in Figure 2.5f.

Moreover, as shown in Figure 2.6a–c, the diffraction patterns of the films at  $-70$  and  $0$  V had clear peaks, whereas that of the

film at +30 V is obscure and had ring-shaped pattern. As can be seen by HRTEM and diffraction pattern images, it can be concluded that the films at -70 and 0V had higher crystallinity than the film at +30 V.

In Figure 2.7, XRR graphs of the films at -70, 0 and +30 V are shown. The first 0.7 degrees of XRR graphs is shown. The critical angle of the films at -70, 0 and +30 V correspond to the inflection point of the graphs and are  $0.31^\circ$ ,  $0.28^\circ$  and  $0.25^\circ$ , respectively. Using the critical angle, the density of the film could be calculated theoretically the equation (1),

$$\alpha_c \approx \sqrt{\frac{r_0 \lambda^2}{\pi} N_A \frac{(Z + f')}{A} \rho} \quad \dots \text{Equation (1)}$$

where  $\alpha_c$  is the critical angle,  $r_0$  is the classical electron radius,  $\lambda$  is the wavelength of Cu-K  $\alpha 1$ ,  $N_A$  is Avogadro's number,  $Z$  is the atomic number of Ti,  $f'$  is the real part of the dispersion coefficient,  $A$  is the atomic weight of Ti and  $\rho$  is the density of the films. The theoretically calculated densities of the films at -70, 0 and +30 V were 4.974, 4.058 and 3.499 g/cm<sup>3</sup>, respectively.

Characteristics of the films at -70, 0 and 30 V are summarized in Table 2.1. As discussed until now, the film at +30 V shows the lowest crystallinity and density among the all films. Comparing



these results and the research of Jeon et al. [52], the film at +30 V would be deposited also by the minute-sized neutral NPs not only by atoms. This means that the neutral NPs had too small size that they could not be observed by HRTEM although they landed on the TEM membrane. If neutral NPs did not exist, the film at +30V was deposited as atom by atom like ALD and should have extraordinarily high crystallinity and density among all three films.

Meanwhile, the film at  $-70$  V had the highest crystallinity and density. This was might be due to the attraction of the positively charged NPs. The positively charged were accelerated toward the substrate by negative bias of  $-70$  V, resulting in forming dense film. Thus, it can be concluded that the behavior of positively charged NPs critically affected the growth of the highly crystalline and dense film in the RF sputtering process.

## **2.4. Conclusion**

Generation of NPs was confirmed during RF sputtering system and the NPs were also confirmed to be positively charged. Under the same condition, effect of charged NPs on film deposition was investigated by applying substrate bias. When negative substrate

bias was applied, thickness of the film increased, whereas it decreased when positive substrate bias was applied. Also, crystallinity and density of the film get higher when negative substrate bias was applied, whereas those of the film get lower when negative substrate bias was applied. These differences might be due to attraction and repelling of the charged NPs by the substrate bias. Conclusively, charged NPs are generated in RF sputtering system and they play an important role to growth of crystalline and dense film.

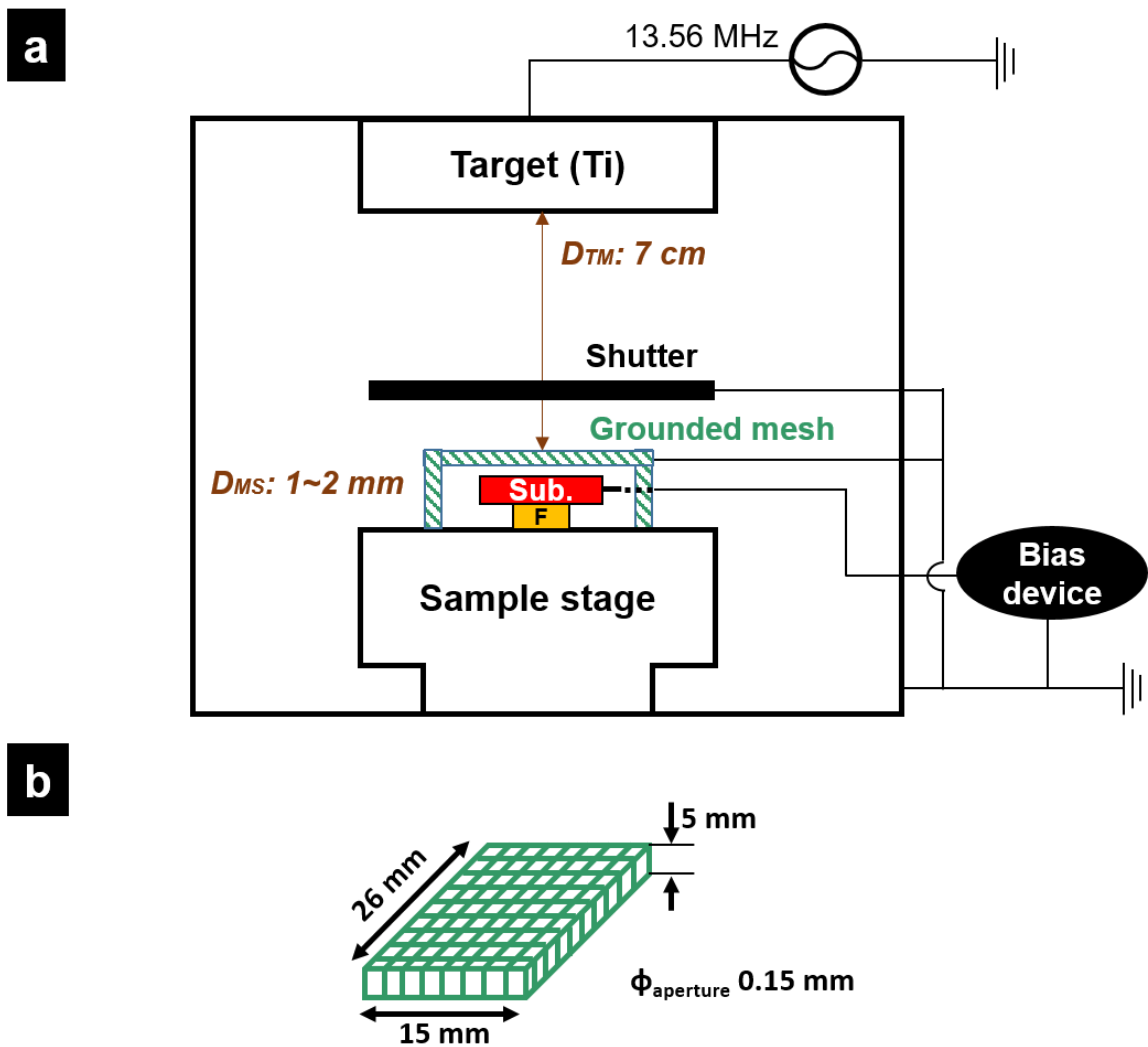


**Figure 2.1.** Schematics of RF sputtering system (a) main chamber  
(b) grounded mesh.

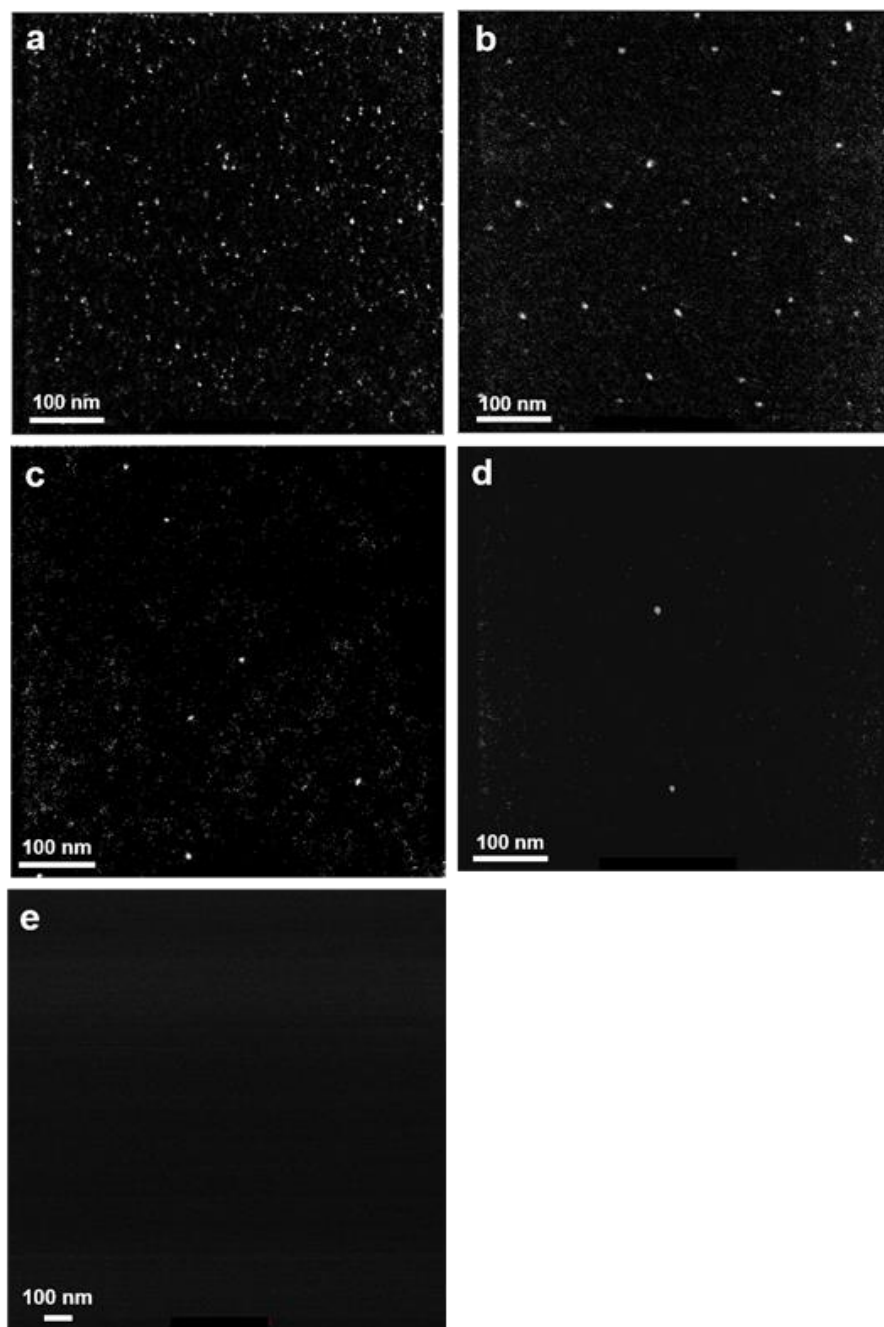


**Figure 2.2.** STEM images of NPs captured on amorphous carbon TEM membranes at the electric bias of (a)  $-70$  V (b)  $0$  V (c)  $+5$  V (d)  $+15$  V and (e)  $+30$  V.

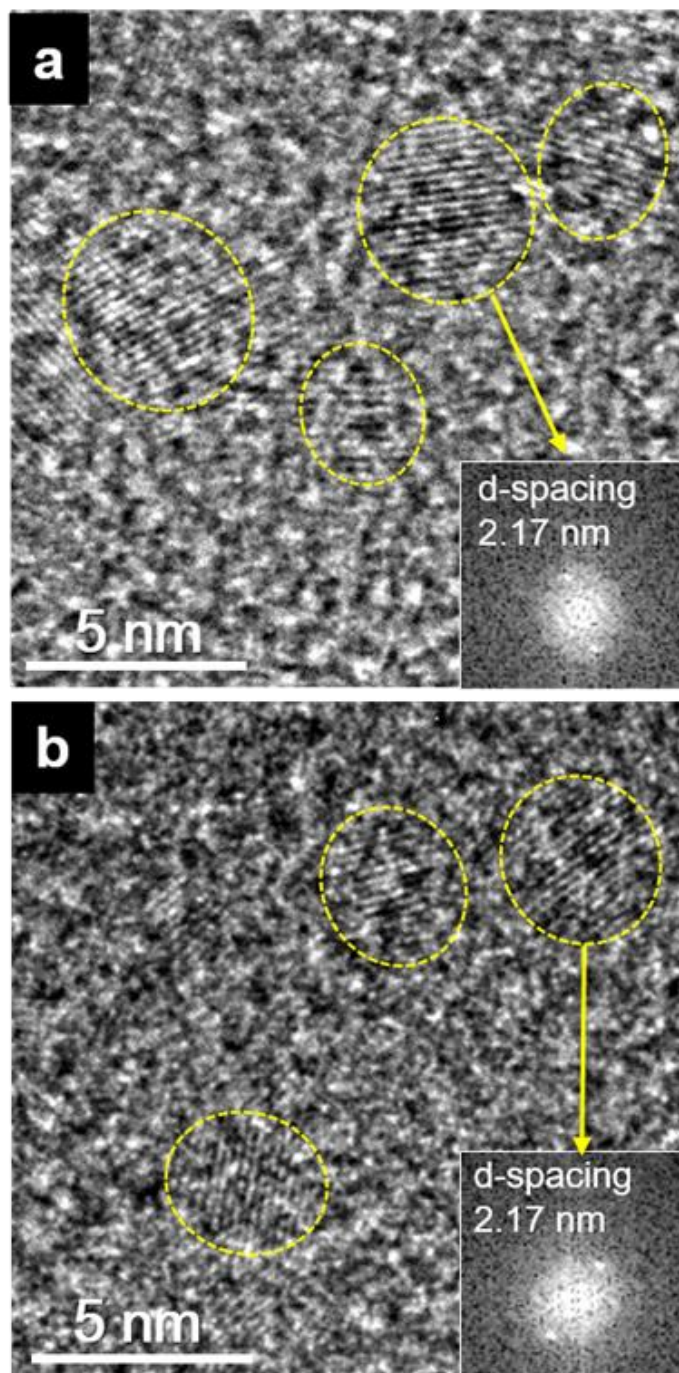


**Figure 2.3.** HRTEM images and fast Fourier transform (FFT) information (inset of the lower right in the image) with d-spacing value of NPs at the electric bias with (a) -70 V and (b) 0 V.

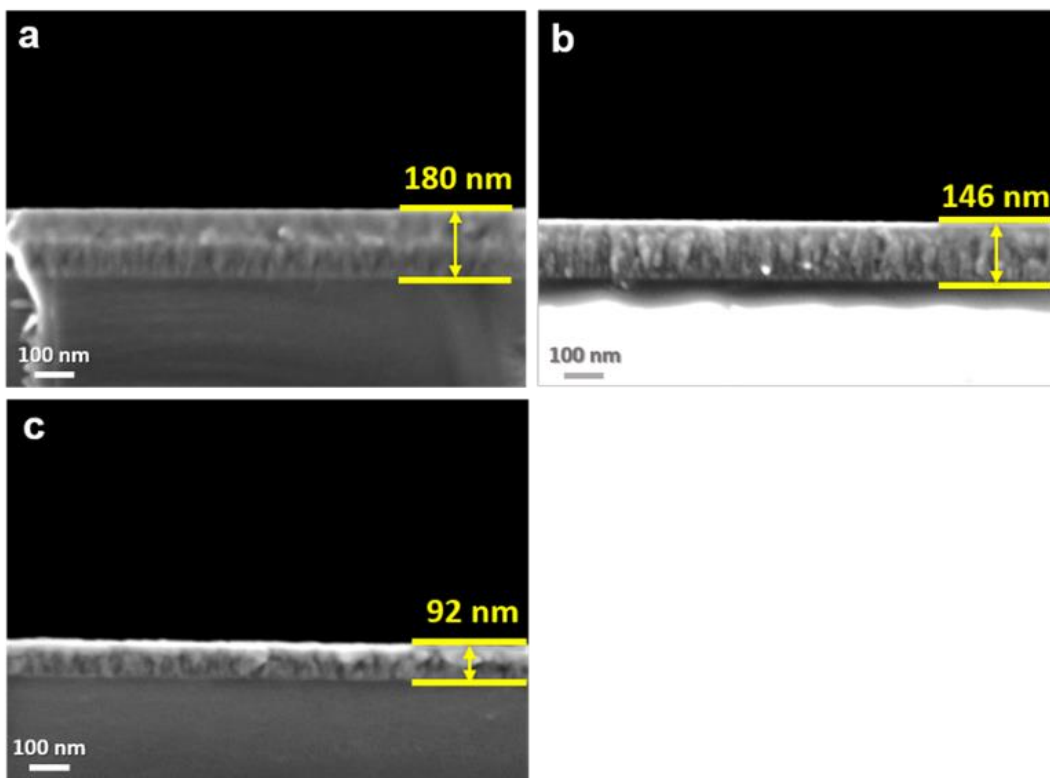


**Figure 2.4.** SEM images of Ti films deposited on Si substrates at the electric bias of (a)  $-70$  V (b)  $0$  V and (c)  $+30$  V.



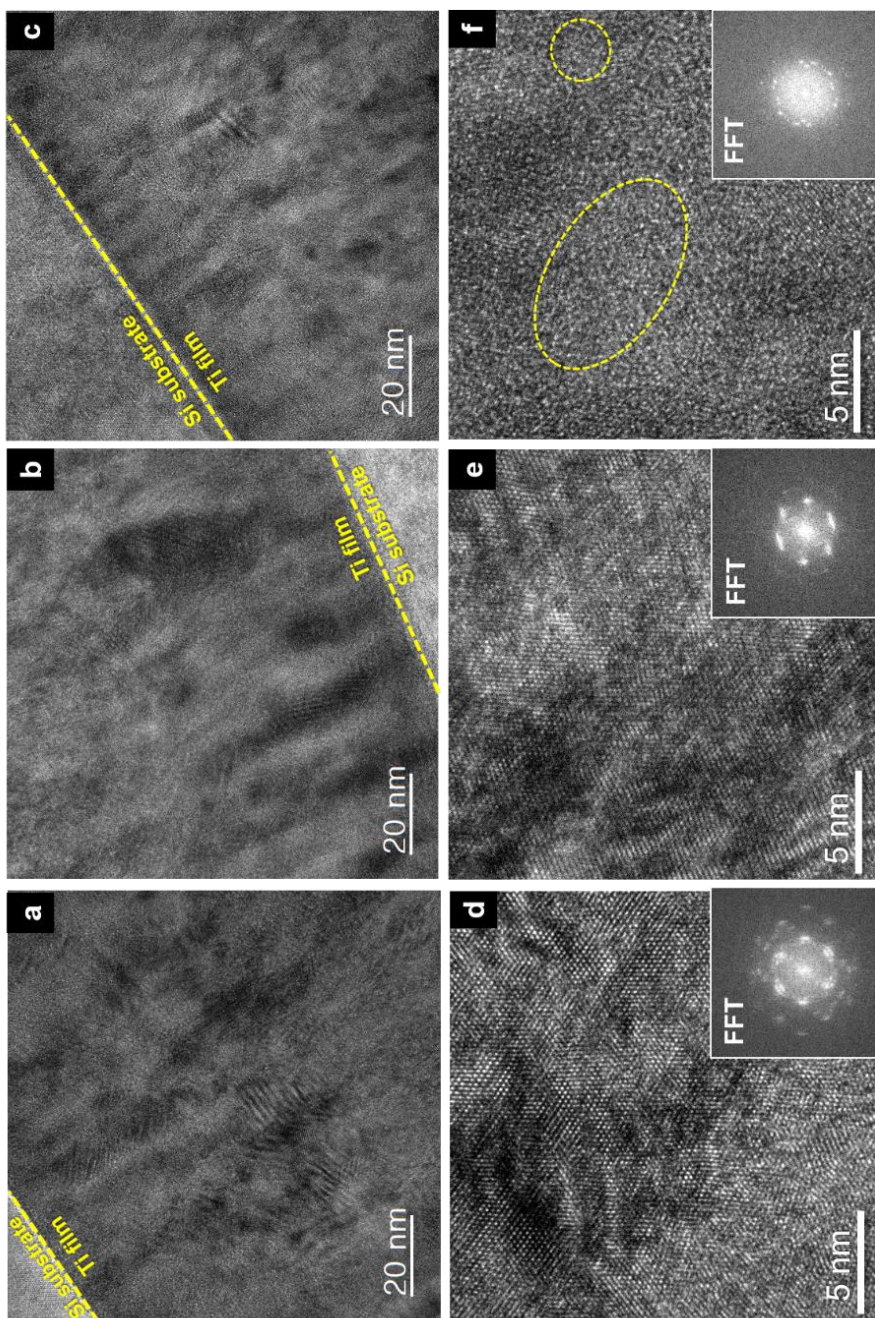


**Figure 2.5.** Low and high magnification TEM images with FFT information (the lower right) of the Ti films deposited on Si substrates at the electric bias of (a), (d)  $-70$  V (b), (e)  $0$  V and (c), (f)  $+30$  V.

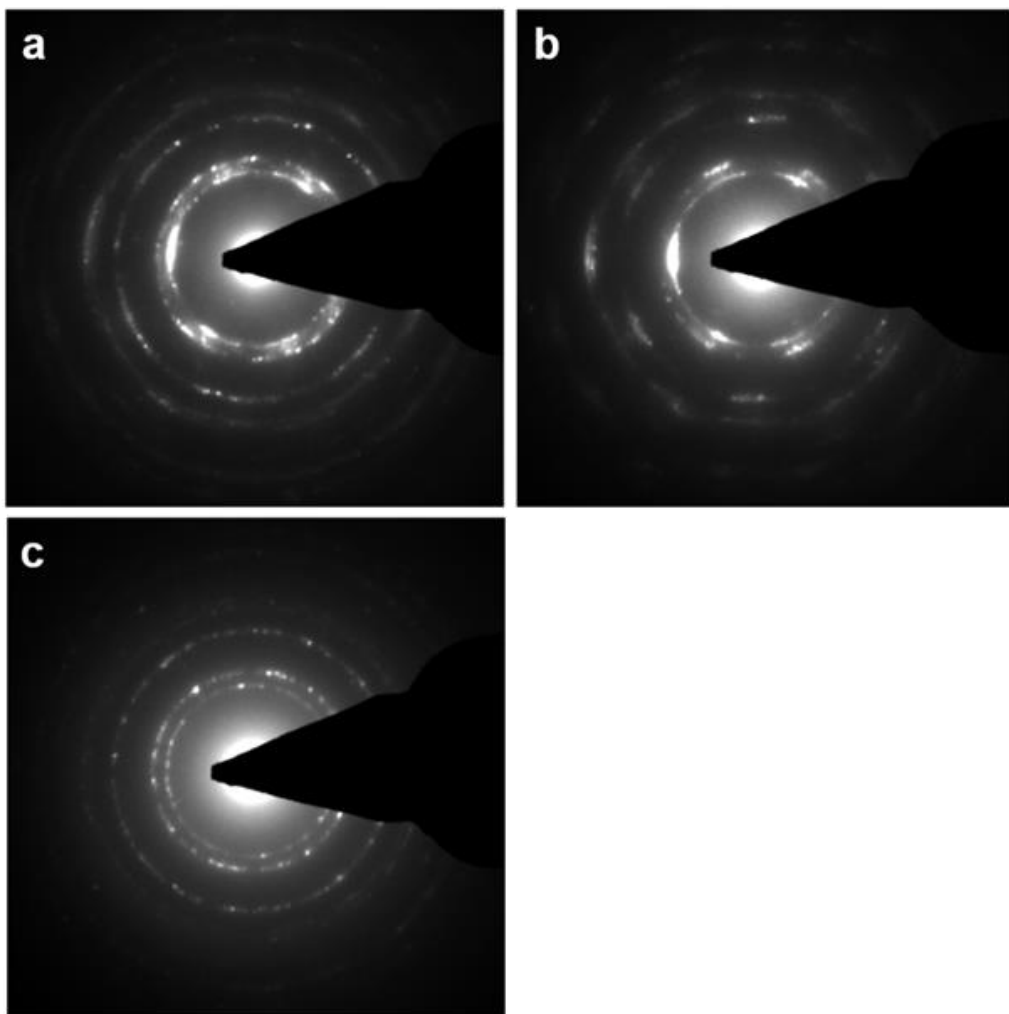


**Figure 2.6.** Diffraction pattern images of the Ti films at the electric bias of (a)  $-70\text{V}$  (b)  $0\text{V}$  and (c)  $+30\text{V}$



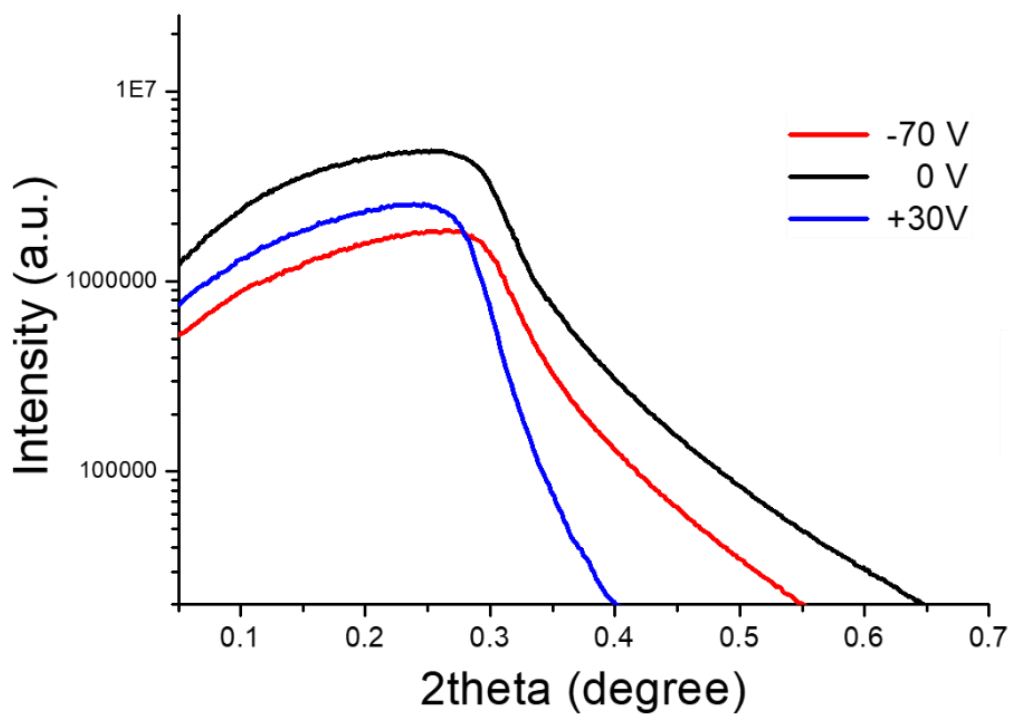


**Figure 2.7.** X-ray reflectivity (XRR) data of the Ti films in the range of  $0^{\circ} \sim 0.7^{\circ}$  at the electric bias of  $-70$  V,  $0$  V and  $+30$  V.

<b>Substrate bias (V)</b>	<b>-70</b>	<b>0</b>	<b>+30</b>
<b>Thickness (nm)</b>	<b>180</b>	<b>146</b>	<b>92</b>
<b>Crystallinity</b>	<b><i>High</i></b>	<b><i>High</i></b>	<b><i>Low</i></b>
<b>Critical angle (°)</b>	<b>0.31</b>	<b>0.28</b>	<b>0.25</b>
<b>Density (g/cm<sup>3</sup>)</b>	<b>4.974</b>	<b>4.058</b>	<b>3.499</b>

Table 2.1. Characteristics of the Ti films with thickness, crystallinity, the calculated density and the measured critical angle by XRR at the electric bias of -70 V, 0 V and +30 V.

# **Chapter 3.**

## **Effect of pressure on the film deposition during RF magnetron sputtering considering charged nanoparticles**

### **3.1. Introduction**

Ti thin films have good biocompatibility and are widely used in biomedical applications [31, 32, 34]. Also, they have outstanding thermal and chemical stability [36] and are widely used in microelectronics [33, 35]. Ti thin films are prepared by direct current (DC) sputtering [37–41, 63], radio frequency (RF) sputtering [43], and high power impulse magnetron sputtering (HiPIMS) [64–66] because of their high reproducibility and growth rate.

Meanwhile, according to the classical crystallization, the

deposition of thin films has been believed to occur by an individual atom, ion or molecule. However, there are some phenomena that cannot be explained by the classical crystallization. Such phenomena can be successfully explained by a new growth mechanism in which thin films grow by a building block of nanoparticles (NPs). This new growth mechanism was supported by many experimental evidences. This new mechanism is referred as ‘non–classical crystallization’ [15, 44–48, 51, 54].

Hwang et al. have extensively studied the nonclassical crystallization of thin films and nanostructures in the chemical vapor deposition (CVD) process [51]. They reported many experimental evidences showing that electrically charged NPs are spontaneously generated in the gas phase in many conventional CVD processes. Most importantly, these charged NPs become a building block of thin films and nanostructures. Hwang et al. emphasized that the charge carried by the NPs played a critical role in the deposition of thin films [52, 53, 57] and nanostructures [56]. They suggested that neutral NPs undergo random Brownian coagulation and produce a porous structure, whereas charged NPs self–assemble and undergo epitaxial recrystallization, consequently producing a dense and crystalline structure. [51] The epitaxial recrystallization indicates that charged NPs undergo liquid–like coalescence, which implies that the bond strength of the NPs should be weakened by

the charge carried by the NPs. According to the ab initio calculation of Clare et al. [20], positive or negative charge in silane ( $\text{SiH}_4$ ) and disilane ( $\text{Si}_2\text{H}_6$ ) molecules weakens significantly the bond strength of Si–H and Si–Si. This new film growth mechanism is called ‘theory of charged NPs (TCN)’ , which turns out to be applicable to many CVD systems. For instance, a negative substrate bias favored the growth of a homoepitaxial SiC film on a SiC substrate during hot wire CVD [67]. Also, a negative substrate bias favored the growth of a fully epitaxial Si film on a Si substrate at a substrate temperature of  $550^\circ\text{C}$  during radio frequency plasma-enhanced CVD [58].

Until now, the generation of charged NPs and their contribution to film growth have been studied mainly in CVD systems. Recently, the generation of negatively charged NPs and their contribution to film growth were studied during DC sputtering of Ag [68] Also, the generation of positively charged NPs and their contribution to film growth was studied during RF sputtering of Ti. [69] Thus, a more systematic study is needed about how the generation of charged NPs is affected by the processing parameter such as pressure in the sputtering process.

The purpose of this study is to confirm how the generation of charged NPs depends on pressure and affects the film deposition

during RF sputtering using a Ti target. To identify the polarity of charged NPs, the electric bias was applied to amorphous carbon membranes for transmission electron microscopy (TEM). The effect of charged NPs on the film deposition was also studied by applying the electric bias to the p-type Si (100) substrate. The growth rate of the films was determined by the cross-section image of field-emission scanning electron microscopy (FESEM) and the crystallinity and orientation of the films were analyzed by X-ray diffraction (XRD).

## **3.2. Experimental method**

Figure 3.1a is a schematic of the RF sputtering system used in this study. A 4-inch Ti target was used and the distance between the target and sample stage was 7 cm. An amorphous carbon TEM membrane (Ted Pella, Inc., Redding, CA, USA) was used as a substrate for capturing NPs and a p-type silicon (100) wafer was used as a substrate for film deposition. The substrate was placed on an insulating polymer sheet for electrical isolation from the sample stage which is grounded. A DC bias device was connected to the substrate for applying the electric bias. In order for the electrical potential of the substrate not to interact with the plasma, a

grounded mesh, which is shown in Figure 3.1b, was installed 1 ~ 2 mm above the substrate. This grounded mesh had the hole size less than Debye length of the plasma [70]. Thus, the same plasma condition could be maintained regardless of the electrical potential of the substrate. In order to capture NPs on a carbon TEM membrane, a round-shaped shutter with 5 cm diameter was installed above the grounded mesh as shown in Figure 3.1a. For capturing NPs, the TEM membrane was exposed to plasma for a few seconds. The exposure time was controlled by the shutter.

Prior to the experiment, the sputtering chamber was evacuated to be less than  $1 \times 10^{-6}$  Torr. For sputtering, RF power was kept at 160 W and Ar gas was used for plasma generation. Pressure was varied from 20 to 80 mTorr. The parameters chosen in this study are those commonly used in the RF sputtering process [71–73]. Since the number density of captured Ti NPs under 80 mTorr was smaller than that under 20 mTorr, the exposure time under 80 mTorr was 8 s and that under 20 mTorr was 5 s to control the number density of NPs appropriate for TEM observation.

To confirm whether the Ti NPs were charged or not, the number density of captured Ti NPs was examined at various electric biases of -30 V, 0 V and +50 V applied to the TEM membrane. Also, to confirm how the pressure affects the ratio of

charged to neutral Ti NPs as well as the deposition behavior of Ti films, the pressure was varied as 20 mTorr, 40 mTorr, 60 mTorr and 80 mTorr and the electrical bias applied to the Si substrates was varied as  $-30$  V,  $-10$  V,  $0$  V and  $+50$  V with the other conditions being the same as those of capturing Ti NPs.

Ti NPs captured on the TEM membrane were analyzed by TEM (FEI, Tecnai F20, Hillsboro, OR, USA). The microstructure of the Ti films was investigated by FESEM (Carl Zeiss, SUPRA, Oberkochen, Germany). TEM and FESEM were operated at accelerating voltages of 200 kV and 2 kV, respectively. The crystallinity and orientation of the films were analyzed by XRD (PANalytical, X'pert-Pro, Almelo, The Netherlands) at  $2\text{-}\theta$  ranges of  $20^\circ \sim 60^\circ$  using Cu-K $\alpha$  wavelength of 0.154 nm.

### **3.3. Results and discussion**

#### **3.3.1. Capturing charged NPs with various pressure during RF sputtering with a Ti target**

To capture and observe charged Ti NPs, a TEM membrane was used as a substrate. Figure 3.2 is high-resolution transmission



electron microscopy (HRTEM) images showing Ti NPs captured on the amorphous carbon TEM membrane at no substrate bias. Ti NPs in Figure 3.2a and b were captured, respectively, for 5 s under 20 mTorr and for 8 s under 80 mTorr. Crystalline Ti NPs in Figure 3.2 are enclosed by dashed ovals to distinguish them from the other area. Crystalline Ti NPs enclosed by dashed ovals were identified by crystalline peaks in the fast Fourier transformation (FFT) image shown as the inset of Figure 3.2.

The majority of the NPs in Figure 3.2 had the average size of  $\sim 3$  nm. The d-spacing values of the NPs determined by the FFT image are mainly 0.212 and 0.216 nm, respectively, for 20 mTorr and 80 mTorr, both of which correspond to the d-spacing values of titanium carbide (TiC). This result indicates that Ti NPs became carbonized. In relation to the possible cause of carbonization, our previous experiments showed that Ti NPs captured on SiO and SiN membranes were also carbonized during TEM observation. Therefore, Ti NPs in Figure 3.2 seemed to be carbonized by carbon contaminants in the TEM chamber when exposed to electron beams. When the electric bias was applied to the substrate, the electric field would be generated between the substrate and the grounded mesh. This electric field would interact with Ti NPs, if charged, which passed through the grounded mesh toward the membrane. Figure 3.3 shows HRTEM images of NPs captured under 20 mTorr

and 80 mTorr at various substrate biases of  $-30$  V,  $0$  V and  $+50$  V. It should be noted that to compare the number density of Ti NPs between electrical biases of  $-30$  V,  $0$  V and  $+50$  V, Figure 3.3 has a lower magnification than Figure 3.2. Each crystalline Ti NP was marked by dashed ovals in Figure 3.3.

In Figure 3.3, the number density of NPs is higher at the negative bias of  $-30$  V than that at  $0$  V under both pressures. In contrast, it is lower at the positive bias of  $+50$  V than that at  $0$  V under both pressures. These results indicate that some of Ti NPs are positively charged. The positively charged NPs would be attracted to the substrate with the bias of  $-30$  V, increasing the number density of Ti NPs captured on the TEM membrane (Figure 3.3a and d). At the same time, they will be repelled by the substrate with the bias of  $+50$  V, decreasing the number density of Ti NPs captured on the TEM membrane (Figure 3.3c and f). In agreement with these results, Kwon et al. reported that the positively charged Ti NPs were generated during Ti RF sputtering [69]. The strong dependence of the number density of Ti NPs on the electrical bias in Figure 3.3 indicates not only that some of Ti NPs are electrically charged but also that they were formed in the gas phase instead of being nucleated on the TEM membrane. Their formation in the gas phase was further supported by the fact that most NPs in Figure 3.3 had the similar size of  $\sim 3$  nm regardless of the substrate bias. If

NPs are nucleated on the membrane, they should have a size distribution instead of the similar size of  $\sim 3$  nm.

As shown in Figure 3.3, the dependence of the number density on the substrate bias is greater under 80 mTorr than under 20 mTorr. When counted from HRTEM images, the number density under 20 mTorr at the substrate biases of  $-30$  V,  $0$  V and  $+50$  V was 134, 103 and 21 per  $100 \times 100$  nm<sup>2</sup>, respectively, whereas that under 80 mTorr at the substrate biases of  $-30$  V,  $0$  V and  $+50$  V was 196, 98 and 0 per  $100 \times 100$  nm<sup>2</sup>, respectively. No Ti NP was observed in Figure 3.3f at the bias of  $+50$  V. In the other area, also, NPs were hardly observed under 80 mTorr at the substrate biases of  $+50$  V.

It should be noted that no observation of crystalline Ti NPs in Figure 3.3f does not mean the absence of Ti NPs. If small neutral Ti NPs exist, they would not only be affected by the electric bias but also lose their crystalline identity after landing on the amorphous carbon membrane because they would accommodate their structure to the amorphous membrane. If small neutral Ti NPs exist, it is difficult to estimate their contribution to film deposition in comparison with the contribution of neutral atoms to film deposition. One possible way to determine which of small neutral NPs and atoms would be a dominant flux for film deposition would be the

quality of the film deposited under the positive bias applied to the substrate. If the film has good crystallinity, atoms would be a dominant flux whereas if the film has a poor crystallinity, small neutral NPs would be a dominant flux. Which of small neutral NPs and atoms would be a dominant flux can be determined by studying the crystallinity of the film deposited under the positive bias. The result will be shown later.

The ratio of the number density for biases of  $-30$  V and  $0$  V was  $1.30$  (Figure 3.3a and b) and  $2.02$  (Figure 3.3d and e), respectively, under  $20$  mTorr and  $80$  mTorr. The larger ratio under  $80$  mTorr indicates that the percentage of positively charged Ti NPs is higher under  $80$  mTorr than under  $20$  mTorr. The reason might be that the collision frequency of NPs with  $\text{Ar}^+$  ions or other positively charged species in the plasma would be higher under  $80$  mTorr because the mean free path under  $80$  mTorr is shorter than that under  $20$  mTorr.

If Figure 3.3 indicates that the percentage of positively charged NPs is higher under  $80$  mTorr than under  $20$  mTorr, the bias effect on the film growth rate would be more pronounced with increasing pressure. To check this possibility, Ti films were deposited on a Si substrate at substrate biases of  $-30$  V,  $-10$  V,  $0$  V and  $+50$  V under  $20$  mTorr,  $40$  mTorr,  $60$  mTorr and  $80$  mTorr.

### 3.3.2. Deposition of Ti thin films under various pressures

Figure 3.4 is the images of FESEM showing cross-sections of Ti films deposited for 15 min under 80 mTorr at biases of  $-30$  V,  $-10$  V,  $0$  V and  $+50$  V. Film thicknesses of Figure 3.4a–d are, respectively, 132, 133, 97 and 29 nm. The film thickness drastically decreased as the bias increased from  $-30$  V to  $+50$  V, indicating that an appreciable percentage of NPs is positively charged. At substrate biases of  $-30$  V and  $-10$  V, positively charged Ti NPs would be attracted toward the substrate, increasing the film growth rate. At the substrate bias of  $+50$  V, however, positively charged Ti NPs would be repelled from the substrate, decreasing the film growth rate. The effect of the substrate bias was most pronounced under 80 mTorr and became less pronounced with decreasing pressure.

Figure 3.5 shows the growth rate of the films deposited under varying biases and varying pressures. The growth rate of films deposited at  $-10$  V is higher than that deposited at  $0$  V under all pressures. The reason would be the attraction of the positively charged Ti NPs to the Si substrate applied with the bias of  $-10$  V. However, the growth rate of films deposited at  $-30$  V was lower than that deposited at  $-10$  V under all pressures except 20 mTorr. Although more Ti NPs would be attracted to the substrate at  $-30$  V

than at  $-10$  V, the incident energy of  $\text{Ar}^+$  ions on the growing surface would be so high at  $-30$  V that the bombardment of  $\text{Ar}^+$  ions would resputter the Ti film, decreasing the growth rate.

On the other hand, the growth rate of films deposited at  $+50$  V is the lowest under all pressures. The reason would be that the substrate bias of  $+50$  V repelled the positively charged Ti NPs from the substrate.

As shown in Figure 3.5, the bias effect on the film growth rate becomes more pronounced as pressure increases. The reason would be that as the pressure increases, the mean free path decreases and the collision frequency of NPs with  $\text{Ar}^+$  and other positively charged species increases; as a result, the percentage of positively charged NPs increases as discussed in Section 3.1.

It should be noted that although Ti NPs were absent at the substrate bias of  $+50$  V in Figure 3.3f, the film growth rate was appreciable at the bias of  $+50$  V in Figure 3.5. Considering Figure 3.3f, the film growth at  $+50$  V in Figure 3.5 comes entirely from the deposition of neutral atoms or NPs. If the film was deposited mainly by neutral atoms at  $+50$  V, it would have good crystallinity whereas if the film was deposited mainly by neutral NPs at  $+50$  V, it would have poor crystallinity. This aspect was studied by Kwon et al. [69],

who reported that neutral NPs produce not only films of poor crystallinity but also films of low density. To determine which of neutral atoms and NPs are the main flux, the crystallinity of films, which can be analyzed by XRD, should be examined.

Figure 3.6 shows XRD data of the films deposited at various substrate biases under various pressures. Under all pressures, the films deposited at the substrate bias of +50 V do not show any clear peak in contrast to the films deposited at the substrate biases of -30 V, -10 V and 0 V. These results indicate that the films deposited at +50 V are almost amorphous or nano-crystalline. From these results, it is confirmed that at the bias of +50 V, the films were deposited not only by neutral atoms but also by neutral clusters.

Meanwhile, the films deposited at the substrate biases of -30 V and -10 V show XRD peaks with (100) orientations of Ti under all pressures, whereas the films deposited at 0 V show either (100) or (002) orientations. This difference is thought to come from the difference in the incident energy of sputtered species on the substrates. According to Kwon et al. [42], the different incident energy on floating and grounded substrates during Ti RF sputtering affected the orientations of the films. The (100) oriented Ti films were obtained with high incident energy whereas the (002)

oriented Ti films were obtained with low incident energy. In this experiment, the positively charged NPs would be accelerated by the substrate biases of  $-30$  V and  $-10$  V, resulting in high incident energy and (100) orientation of the films. In contrast, in the case of  $0$  V, the incident energy was relatively low, resulting in either (100) or (002) orientation.

### **3.4. Conclusion**

Positively charged Ti NPs were spontaneously generated during the RF sputtering process. The ratio of charged to neutral Ti NPs increased as the pressure increased. The negative substrate bias increased the growth rate of the films, which is attributed to attracting positively charged Ti NPs, whereas the positive substrate bias decreased the growth rate of the films, which is attributed to repelling them. Such a bias effect became pronounced as the pressure increased.



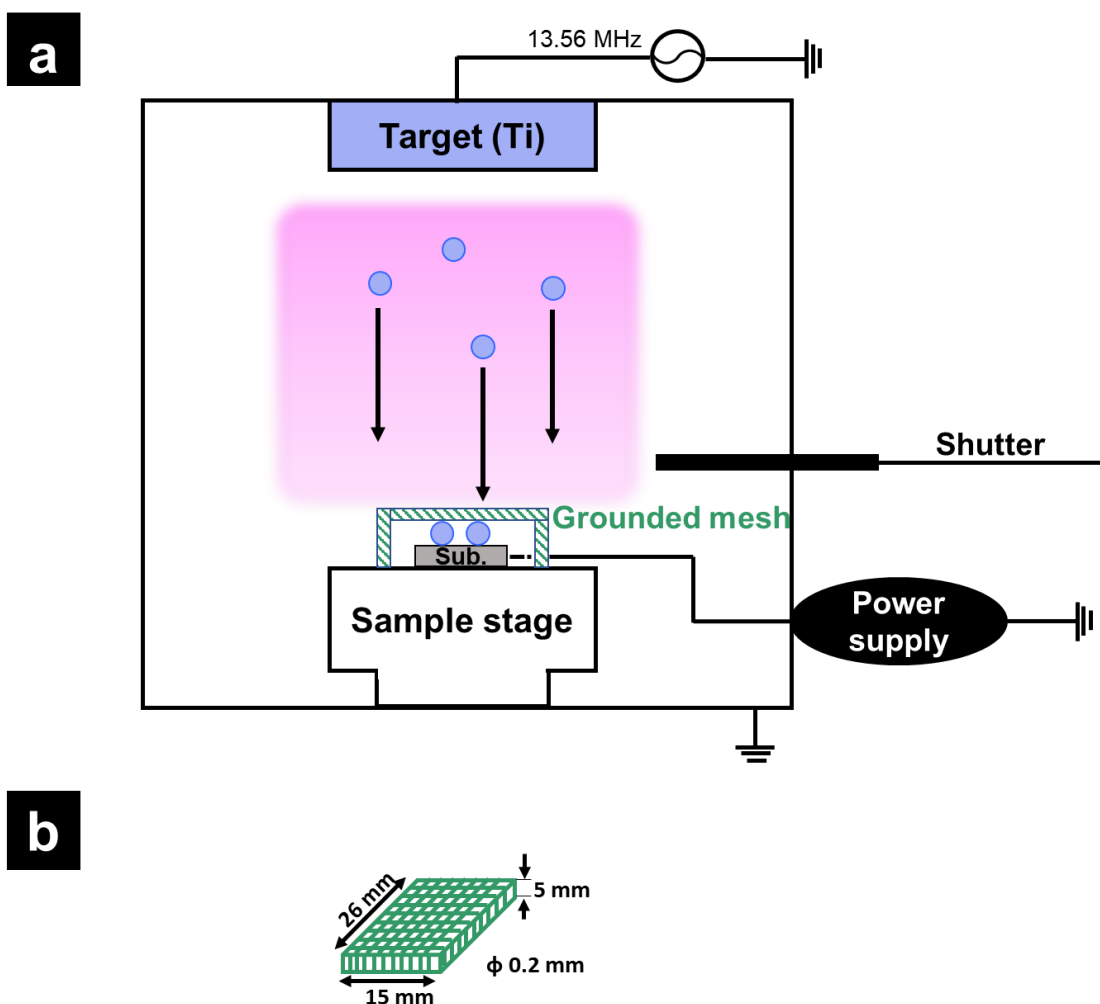


**Figure 3.1.** Schematics of RF sputtering system (a) main chamber  
(b) grounded mesh

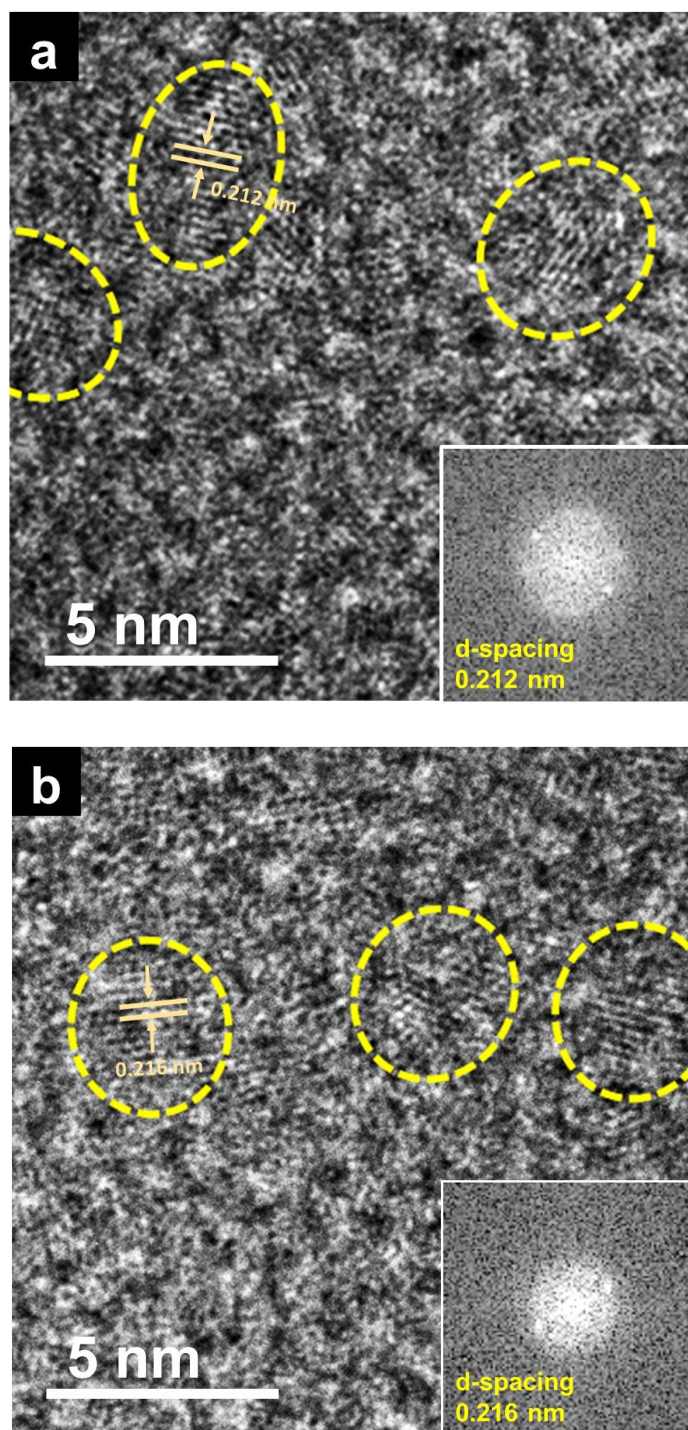


**Figure 3.2.** HRTEM images and FFT information (inset of the lower right in the image) with d-spacing value of NPs at the substrate bias of 0 V under (a) 20 mTorr and (b) 80 mTorr.

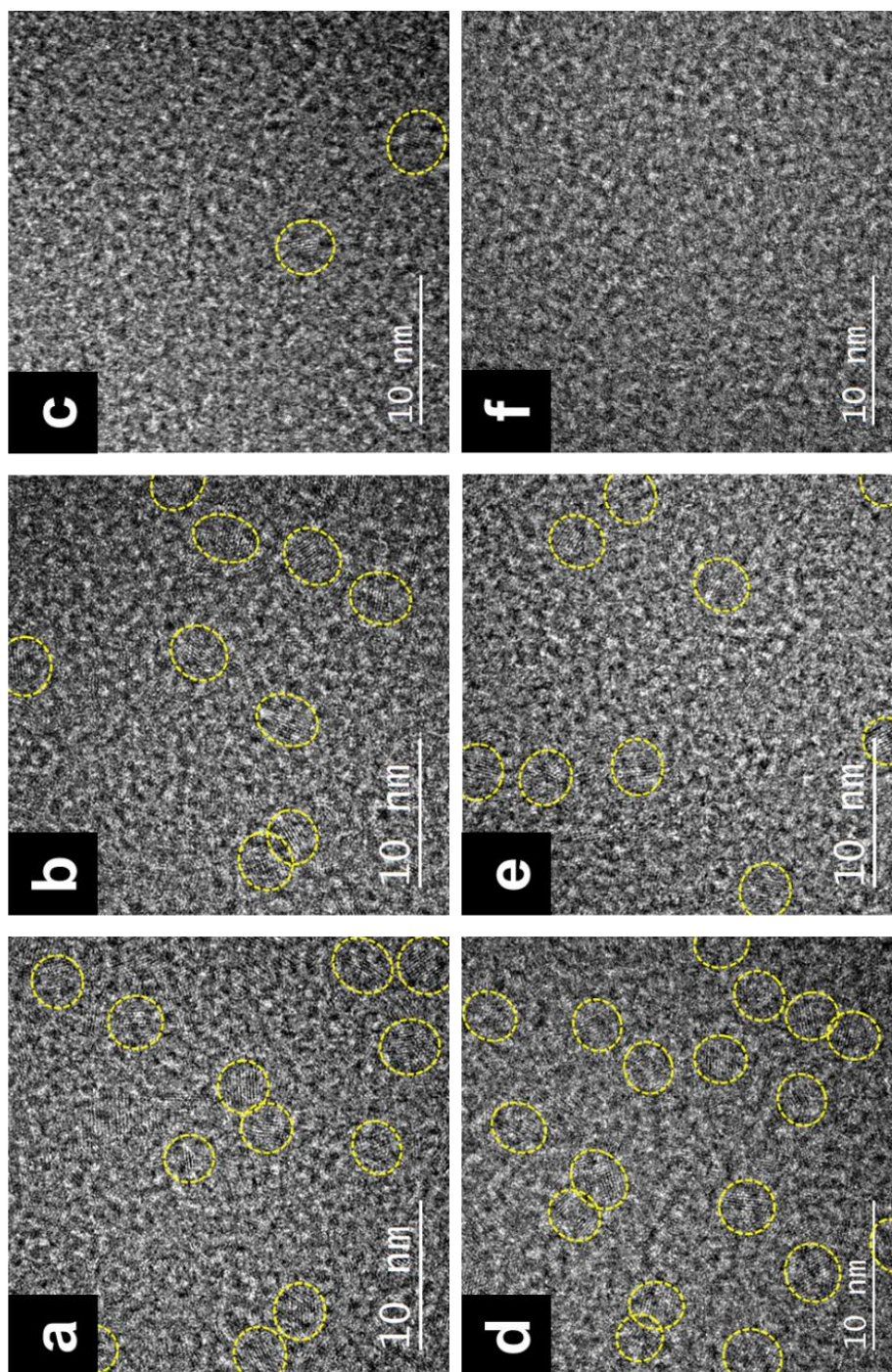


**Figure 3.3.** HRTEM images of NPs at the substrate bias of (a)  $-30$  V, (b)  $0$  V and (c)  $+50$  V under  $20$  mTorr and (d)  $-30$  V, (e)  $0$  V and (f)  $+50$  V under  $80$  mTorr.



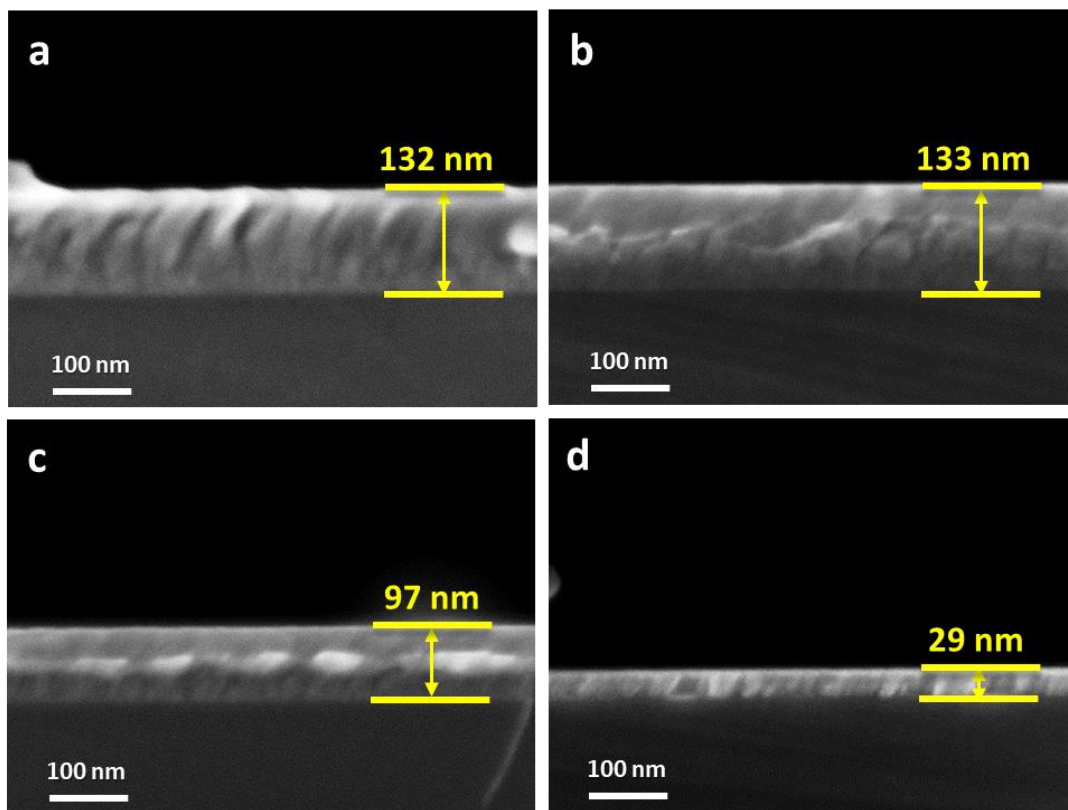


**Figure 3.4.** SEM images of the Ti films deposited on Si substrates under 80 mTorr at biases of (a)  $-30$  V (b)  $-10$  V (c)  $0$  V and (d)  $+50$  V.

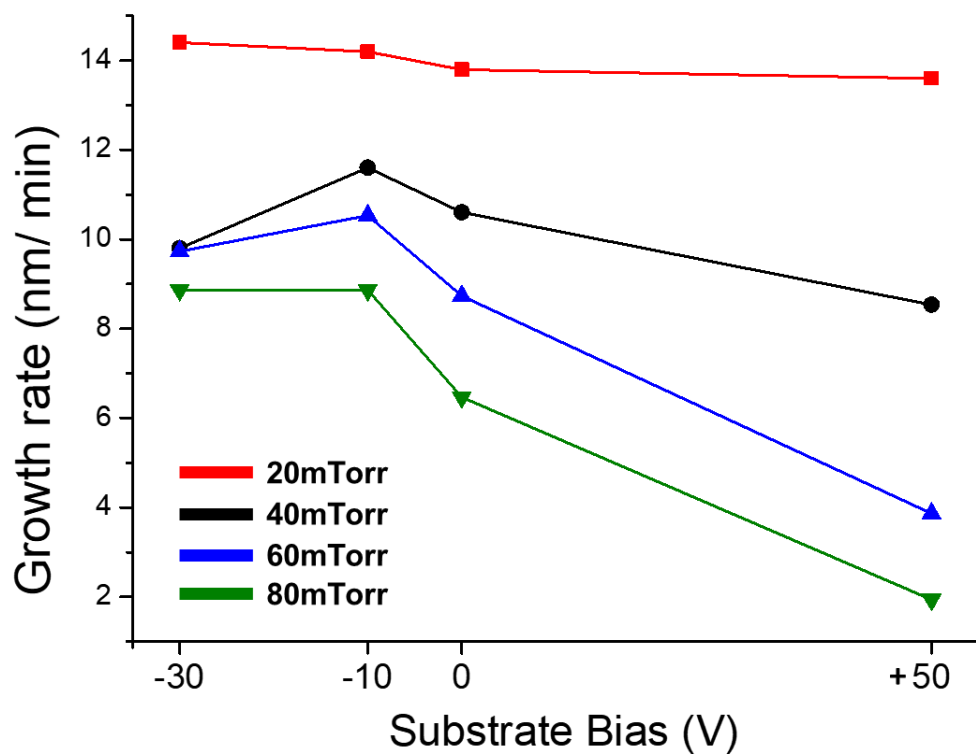


**Figure 3.5.** Growth rate of the Ti films deposited at the substrate bias of  $-30$  V,  $-10$  V,  $0$  V and  $+50$  V under 20 mTorr, 40 mTorr, 60 mTorr and 80 mTorr.

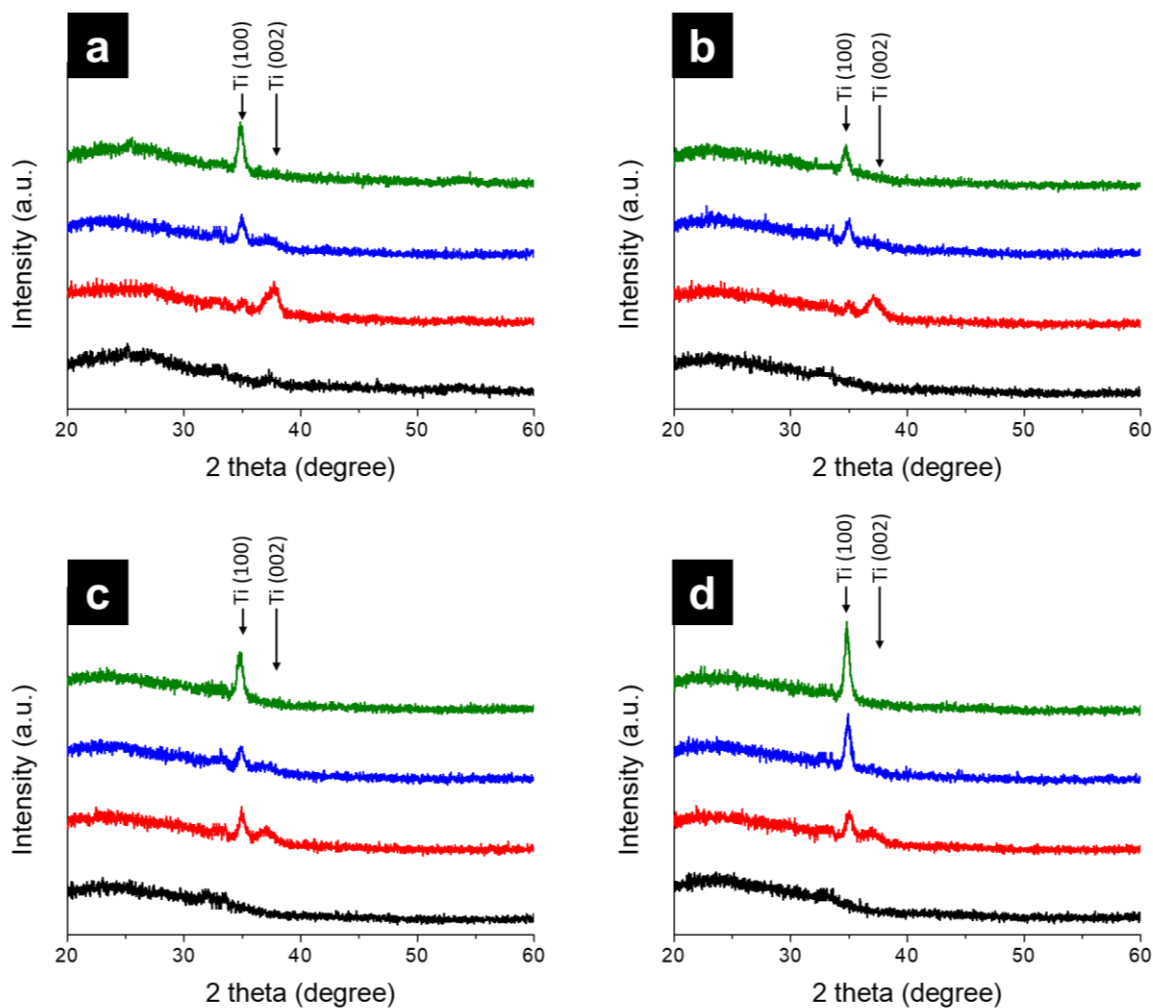


**Figure 3.6.** XRD data of the Ti films deposited at the substrate bias of  $-30$  V,  $-10$  V,  $0$  V and  $+50$  V under (a) 20 mTorr, (b) 40 mTorr, (c) 60 mTorr and (d) 80 mTorr.

# **Chapter 4.**

## **Methods for growing low-resistivity tungsten film by controlling charged nanoparticles**

### **4.1. Introduction**

Tungsten is a heavy and very hard transition metal, which is produced from wire manganese lite and scheelite. Among the elements, it has the highest melting point, and its density is  $19.3\text{g/cm}^3$ , which is similar value to gold or uranium. Pure tungsten is hard and has excellent ductility, and when a small amount of impurities is added, it is hard but brittle and difficult to process. Pure tungsten is used in the electronic fields but is mainly used as a compound or alloy. The filament of the bulb is the most representative. Also, since tungsten is hard and dense, it is widely used for bullets that pierce the armor of tanks for military purposes.

However, if impurities are slightly mixed, there is a disadvantage that it becomes hard and brittle. Tungsten has the highest melting point of all elements, which is  $3422^{\circ}\text{C}$  and the lowest vapor pressure, which is above  $1650^{\circ}\text{C}$ . Although the temperature at which carbon exists in a solid state is higher, tungsten is an element with the highest melting point because carbon does not pass through a liquid state at about  $4027^{\circ}\text{C}$  and immediately sublimates into gas. In addition, the tensile strength of tungsten is the highest among all elements because the electrons of the 5d orbital strongly bond tungsten atoms to each other.

In addition, tungsten has two kinds of atomic arrangements. One is  $\alpha$  tungsten, which has a body-centered cubic structure and is the most stable among tungsten structures.  $\beta$  tungsten has an A15 equiaxed crystal structure, which is shown in Figure 4.1. This structure is a metastable phase and can exist with the  $\alpha$  structure in a general state. The  $\alpha$  structure has an electrical resistance of  $1/3$  of that of the  $\beta$  structure, and the critical temperature at which it becomes a superconductor is about  $0.015\text{K}$ , which is lower than that of  $1\sim 4\text{K}$  in the  $\beta$  structure. When the two types of structures are mixed, the critical temperature is intermediate. Alloys made from a mixture of tungsten and other metals exhibit higher critical temperatures, which are used in low-temperature superconductor circuits.



Tungsten thin films are also used in metallization field. As semiconductor devices are miniaturized, the line width of the currently used copper interconnect is also decreasing. However, as the line width decreases, the resistivity rapidly increases, that is, the resistivity size effect appears seriously in the case of copper. Meanwhile, tungsten has a shorter electron mean free path than copper. Because the resistivity size effect can be reduced as the electron mean free path get shorter, tungsten is replacing the copper interconnects and now generally used.

Meanwhile, in the earlier sections, the generation of charged NPs and their effect on film deposition during RF magnetron sputtering was discussed. Also, the effect of charged NPs on film deposition get pronounced as the pressure increases. In this context, this understanding of charged NPs can be applied to deposit of tungsten film with the purpose of decreasing resistivity of the film. If the resistivity of tungsten film can be reduced using the understanding of charged NPs, it could be a good example to show that the control of charged NPs is another critical factor to enhance the film quality. Thus, applicability of the theory of charged NPs is investigated in this chapter.

RF magnetron sputtering which is used in this study is selected to increase the ionization rate of plasma that is used to deposit film.

The ionization rate of RF magnetron sputtering is higher than that of DC magnetron sputtering because of electron oscillation. The higher ionization rate is favored to induce the charging of NPs, which results in enhancing the film quality. Thus, if the ionization rate can be higher than that of RF magnetron sputtering, the film quality is expected to be enhanced more. High power impulse magnetron sputtering (HiPIMS) is known to have higher ionization rate than conventional sputtering. Thus, it is well expected to induce more charging of NPs using HiPIMS than RF magnetron sputtering, which can enhance the film qualities like resistivity. Thus, films were deposited with HiPIMS and the qualities of the films were compared with those of the films deposited with RF magnetron sputtering also in this chapter.

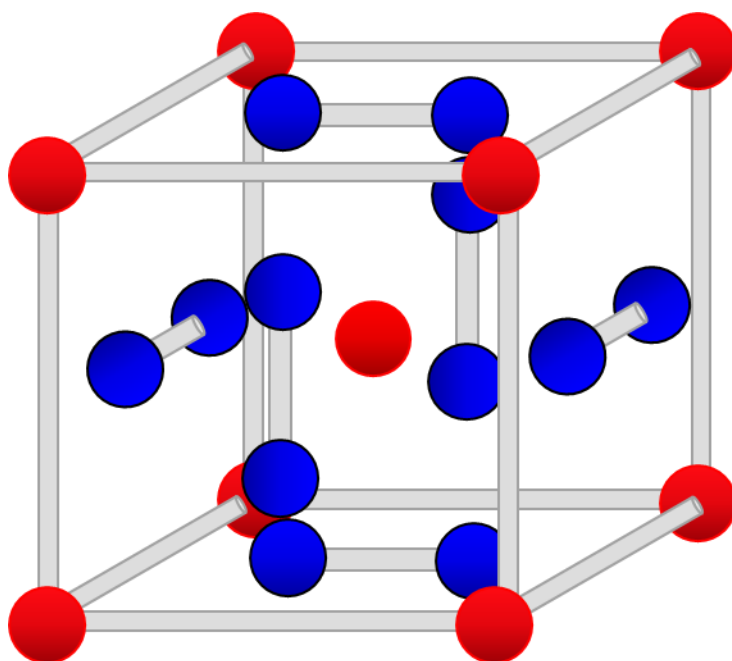


**Figure 4.1.** Crystal structure of A-15  $\beta$  tungsten.

## 4.2. Experimental method

Figure 4.2a is a schematic of the RF magnetron sputtering system used in this chapter. A 2-inch tungsten target was used and the distance between the target and sample stage was 7 cm. An amorphous carbon TEM membrane (Ted Pella, Inc., Redding, CA, USA) was used as a substrate for capturing NPs and a p-type silicon (100) wafer with  $1 \times 1 \text{ cm}^2$  size was used as a substrate for film deposition. An insulating polymer sheet was placed between the substrate and the sample stage for electrical isolation because the sample stage is grounded. A DC bias device was connected to the substrate for applying the electric bias. To separate the substrate and plasma, a grounded mesh, which is shown in Figure 4.2b, was installed  $1 \sim 2 \text{ mm}$  above the substrate. With this grounded mesh, the electrical potential of the substrate did not interfere with the plasma. Thus, the same plasma condition could be maintained regardless of the electrical potential of the substrate. For this purpose, the grounded mesh had the hole size less than Debye length of the plasma [70].

In order to capture NPs on a carbon TEM membrane, it should be exposed to plasma for a few seconds. With a longer exposure time, films will be deposited on the membrane not NPs. To control

exposure time, a round-shaped shutter with 5 cm diameter was installed above the grounded mesh as shown in Figure 4.2a.

Prior to the experiment, the sputtering chamber was evacuated to be less than  $1 \times 10^{-6}$  Torr. For sputtering, RF power was kept at 40 W and Ar gas was used for plasma generation. Pressure was varied from 5 to 80 mTorr. Tungsten NPs were capture with substrate bias of -70, 0, +50 V. Also, tungsten films were deposited with substrate bias of -70, -30, -10, 0 and +50 V.

Experimental setting for HiPIMS is shown in Figure 4.3. It was very similar to that of RF magnetron sputtering although different chamber was used. Power supply for HiPIMS was connected to target. A 3-inch tungsten target was used and the distance between the target and sample stage was 14 cm. A p-type silicon (100) wafer with 1 x 1 cm<sup>2</sup> size was used as a substrate for film deposition. For sputtering, average power was 0.5 kW and 0.7 kW. Ar gas was used for plasma generation and pressure was 0.5 Pa, 0.7 Pa and 0.9 Pa. Experiment to capture tungsten NPs was not conducted because it was impossible to install the grounded mesh and the shutter that was used during RF magnetron sputtering.

Tungsten NPs captured on the TEM membrane during RF magnetron sputtering were analyzed by TEM (FEI, Tecnai F20,

Hillsboro, OR, USA). The microstructure of the tungsten films was investigated by FESEM (Carl Zeiss, SUPRA, Oberkochen, Germany). TEM and FESEM were operated at accelerating voltages of 200 kV and 2 kV, respectively. The crystallinity and orientation of the films were analyzed by XRD (PANalytical, X' pert-Pro, Almelo, The Netherlands) at 2-theta ranges of  $20^{\circ} \sim 60^{\circ}$  using Cu-K $\alpha$  wavelength of 0.154 nm.

## **4.3. Results and discussion**

### **4.3.1. Tungsten film deposited by RF magnetron sputtering**

The main purpose of this chapter was to reduce resistivity of tungsten film based on the understanding of charged NPs. For this, tungsten films were deposited on silicon substrates with various substrate bias and the resistivity of the films were measured. The results are shown in Figure 4.4. Compared to resistivity of the film deposited with 0 V, resistivity of the film with positive substrate bias is higher. Especially, resistivity with + 50 V under 80 mTorr is much higher than the others. For more detail, the rescaled graph is shown in Figure 4.5. Under all pressure, resistivity with positive

bias is higher than those with 0 V, whereas resistivity with negative bias is lower than those with 0 V. As the more negative bias was applied, resistivity of the films gets lower. This might be due to the existence of positively charged tungsten NPs. It will be discussed with capture experiment. Like the discussion of chapter 3, the bias effect gets pronounced as the pressure is high.

Figure 4.6 is a graph showing the XRD result of the thin film according to the bias by pressure. Currently, two phases of tungsten have been observed. To explain this for a moment, tungsten is a stable phase, alpha tungsten having a BCC structure exists, and beta tungsten as shown in Figure 4.1 exists as a metastable phase. Since this beta tungsten has higher resistivity than alpha tungsten, it is necessary to prevent the formation of beta tungsten in order to lower the target resistivity. On the other hand, it is reported that these studies on the formation of beta tungsten appear when the process pressure is increased and the sputtering power is decreased. That is, beta tungsten is formed under low energy conditions of particles incident on the substrate, and alpha tungsten is produced under high energy conditions. Looking at Figure 4.6 again from this point of view, looking at the 0 V samples without bias, when the pressure is high, the pick of beta tungsten dominates. In other words, when no bias is applied, the formation of beta tungsten can be prevented by using a low pressure. In Figure

4.5, the lower the pressure, the lower the resistivity. However, even in the case of 80 mTorr with increased pressure, when negative bias is applied, the same resistivity as 5mTorr with low pressure can be obtained. Considering this based on the understanding obtained in Chapter 3, it seems that the charging rate of nanoparticles increased as the pressure increased, and the incident energy increased due to attraction to the substrate. In other words, by inducing charging of nanoparticles, low resistivity can be obtained even at high pressure, and the growth rate of 80 mTorr is approximately 30 % higher than that of 5mTorr. In other words, by inducing charging of nanoparticles, a thin film with low resistivity could be obtained at a high growth rate.

#### 4.3.2. Tungsten film deposited by HiPIMS

For HiPIMS experiment, pressure and power were varied. Pressure of 0.5 Pa, 0.7 Pa and 0.9 Pa was used and average power of 0.5 kW and 0.7 kW was used. However, the films under 0.5 Pa were peeled out. Under the other 4 conditions, the films were well deposited. This is summarized in table 4.1.



	0.5 Pa	0.7 Pa	0.9 Pa
0.5 kW	X	O	O
0.7 kW	X	O	O

**Table 4.1.** Summary of results of HiPIMS

Films were deposited for 30 min. FESEM cross-section images of the films are shown in Figure 4.7. Figure 4.7.a and b were films under 0.7 Pa and 0.9 Pa, respectively, with 0.5 kW. Figure 4.7.c and d were films under 0.7 Pa and 0.9 Pa, respectively, with 0.7 kW. The films under higher pressure and higher power shows high growth rate.

Also, FESEM top-view images of the films are shown in Figure 4.8. Figure 4.8.a and b were films under 0.7 Pa and 0.9 Pa, respectively, with 0.5 kW. Figure 4.8.c and d were films under 0.7 Pa and 0.9 Pa, respectively, with 0.7 kW. Sharp edges are observed under all conditions, but there was little difference between the conditions.

Resistivity and roughness of the films were measured and these are shown in Figure 4.9. The roughness of the films does not show a big difference, whereas the resistivity of the films shows much obvious difference. The film deposited under 0.7 Pa with 0.7 kW shows the lowest resistivity. Because the purpose of this chapter is

to reduce the resistivity of the films, we applied additional experimental setting under this condition.

The substrate bias of  $-10$ ,  $-20$ ,  $-30$  V was applied under  $0.7$  Pa with  $0.7$  kW. FESEM cross-section images of the films are shown in Figure 4.10. Figure 4.10.a, b, c and d are respectively the films deposited with substrate bias of  $0$ ,  $-10$ ,  $-20$  and  $-30$  V. the films with  $-10$  V shows the highest growth rate and when negative bias becomes bigger, the growth rate slightly decrease. This might be attributed to attraction of positively charged tungsten NPs.

Also, FESEM top-view images of the films are shown in Figure 4.11. Figure 4.11a, b, c and d are respectively the films deposited with substrate bias of  $0$ ,  $-10$ ,  $-20$  and  $-30$  V. With top-view image, the films do not show an obvious difference.

Resistivity and roughness of the films were measured and these are shown in Figure 4.12. The roughness of the films does not show an obvious difference. However, when the substrate bias of  $-20$  and  $-30$  V was applied, the resistivity of the films decreased. The film deposited with  $-20$  V shows the lowest resistivity.

#### 4.3.3. Comparison of the results of RF sputtering and HiPIMS

The purpose of this chapter was to reduce the resistivity of tungsten films with high ionization rate by HiPIMS. To compare the results of RF magnetron sputtering and HiPIMS, growth rate, resistivity and FWHM of the all films were measure. Figure 4.13 shows the growth rate and resistivity of all films deposited by HiPIMS and RF magnetron sputtering. The films deposited by HiPIMS show higher growth rate and higher resistivity than those deposited by RF magnetron sputtering. We expected that the films deposited by HiPIMS would show lower resistivity, but the results do not match with the expectation. However, the condition that used to deposit films by HiPIMS is the condition that the growth rate is much higher than that of RF magnetron sputtering. They were almost 5 times higher than those of RF magnetron sputtering. Thus, if the condition is optimized, the resistivity is expected to be more decreased.

Figure 4.14 is the XRD analysis of all films and the FWHM of the XRD graph is shown in the below table. The XRD analysis also show that the crystallinity of the films deposited by RF magnetron sputtering is better than those of HiPIMS. This also seems to be because of high growth rate of HiPIMS. If the condition is optimized, crystallinity will be improved.

## 4.4. Conclusion

Tungsten films were deposited by RF magnetron sputtering and HiPIMS. During RF magnetron sputtering, the resistivity of films was reduced by applying negative substrate bias. During HiPIMS, the resistivity of films was also reduced by applying negative substrate bias. However, contrary to expectations, the resistivity of the films deposited by HiPIMS was higher than that of the films deposited by RF magnetron sputtering. This might be attributed to higher growth rate of HiPIMS than that of RF magnetron sputtering. It is expected that the resistivity of films deposited by HiPIMS could be more reduced if the process condition is optimized.

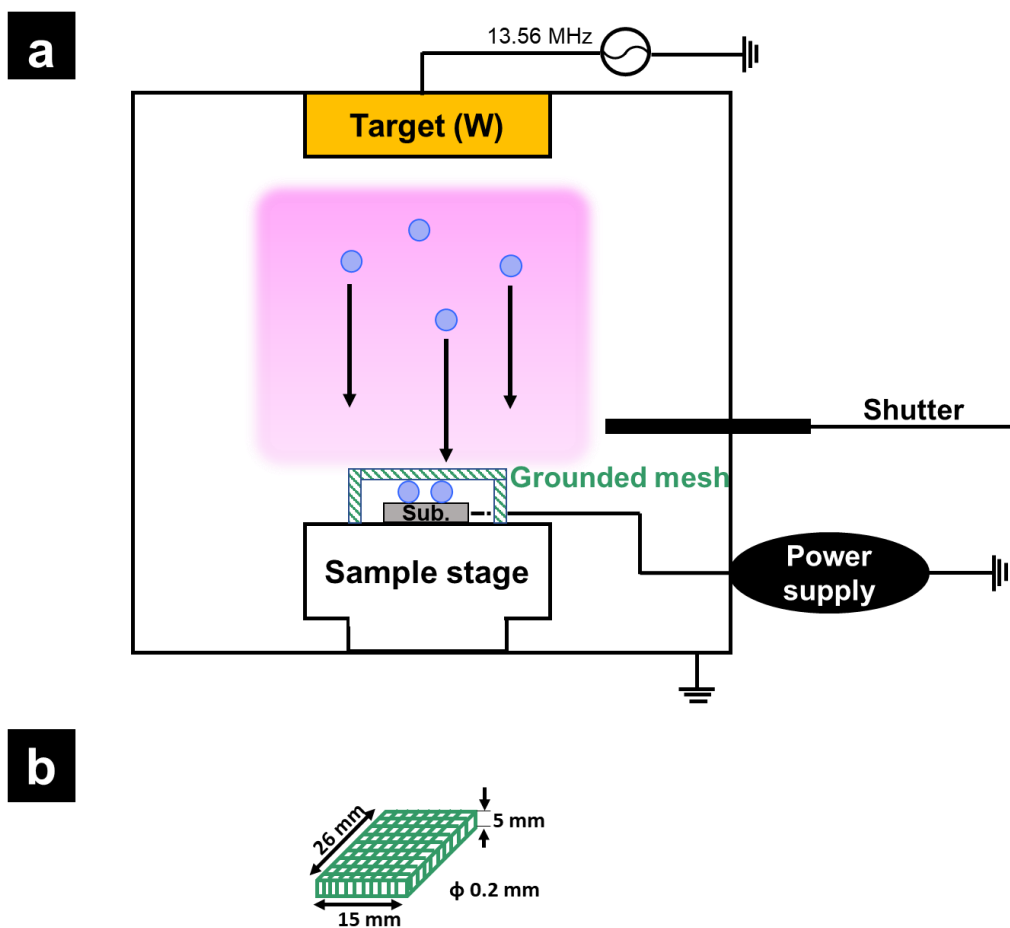


**Figure 4.2.** Schematics of RF sputtering system (a) main chamber  
(b) grounded mesh.

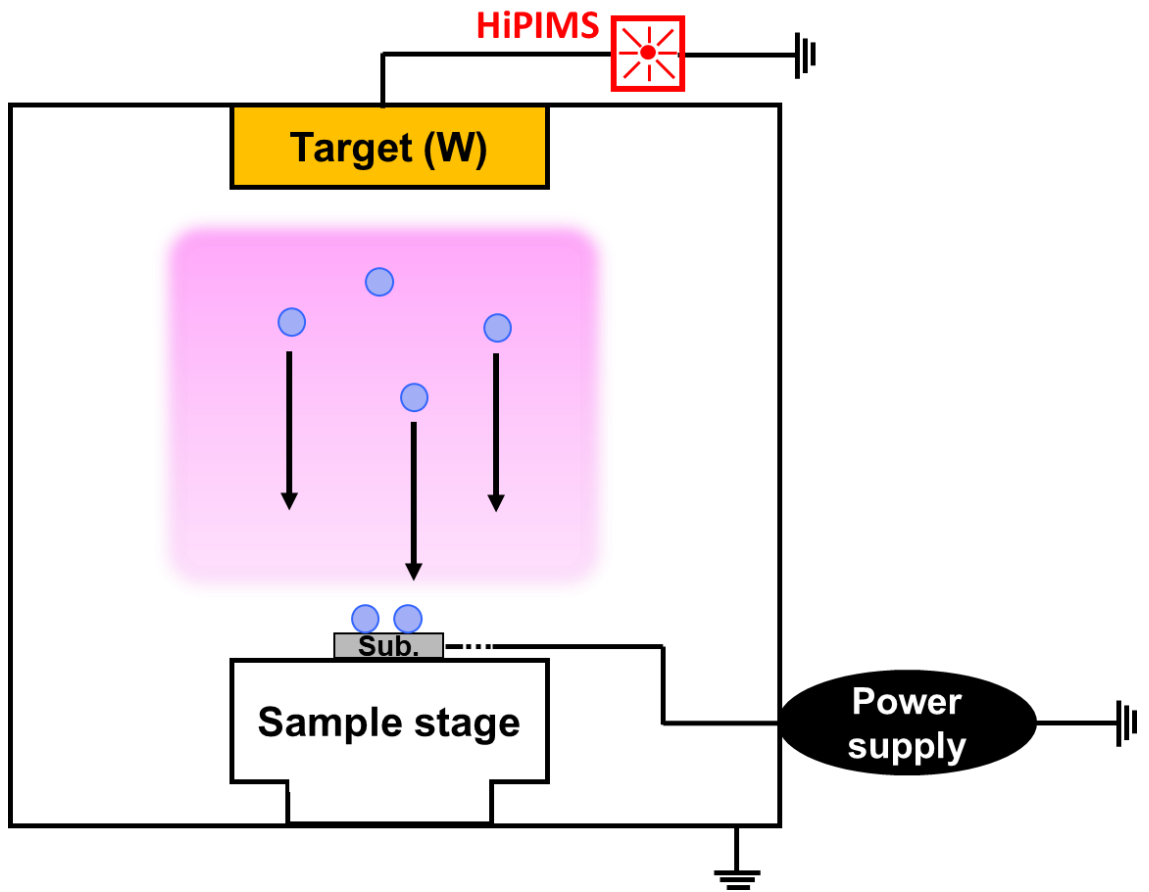
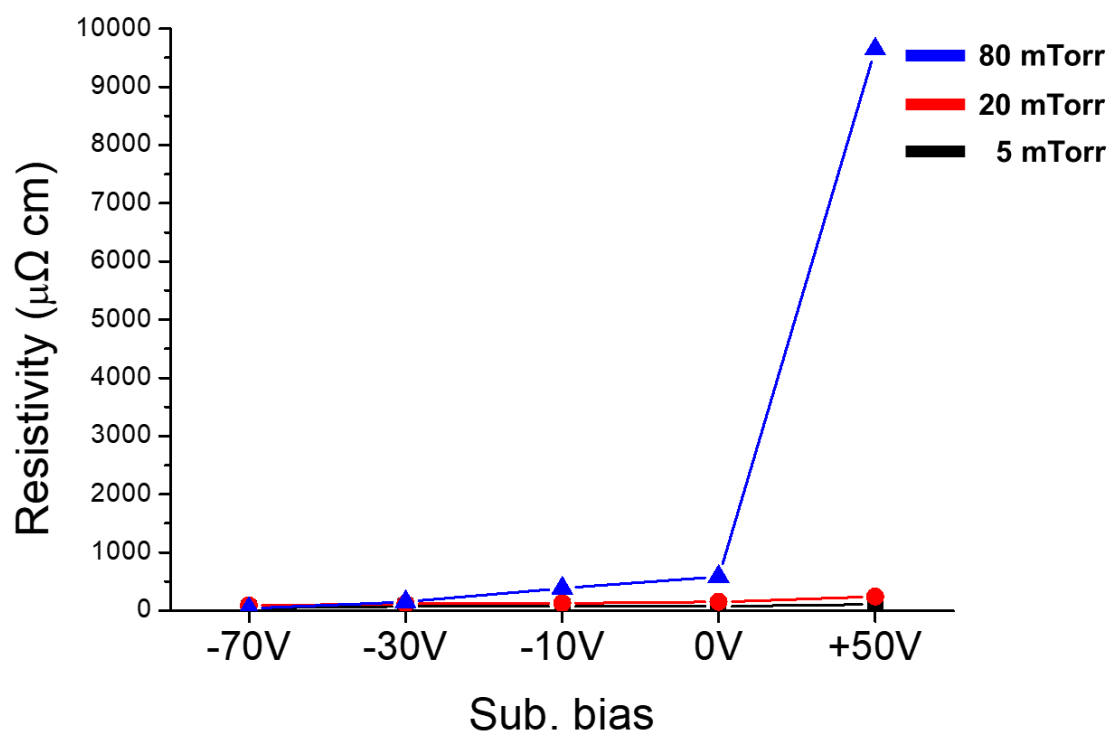
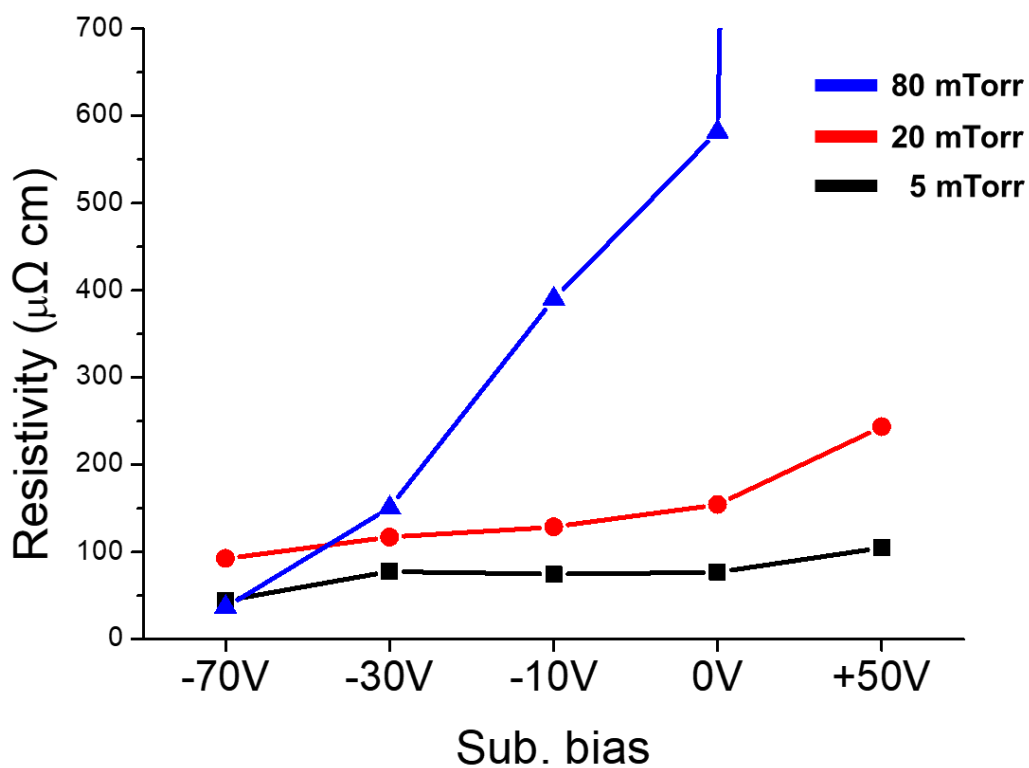


Figure 4.3. Schematics of HiPIMS system.



**Figure 4.4.** Resistivity of the films deposited by RF magnetron sputtering under 5 mTorr, 20 mTorr and 80 mTorr.



**Figure 4.5.** Enlarged graph of the resistivity of the films deposited by RF magnetron sputtering under 5 mTorr, 20 mTorr and 80 mTorr.



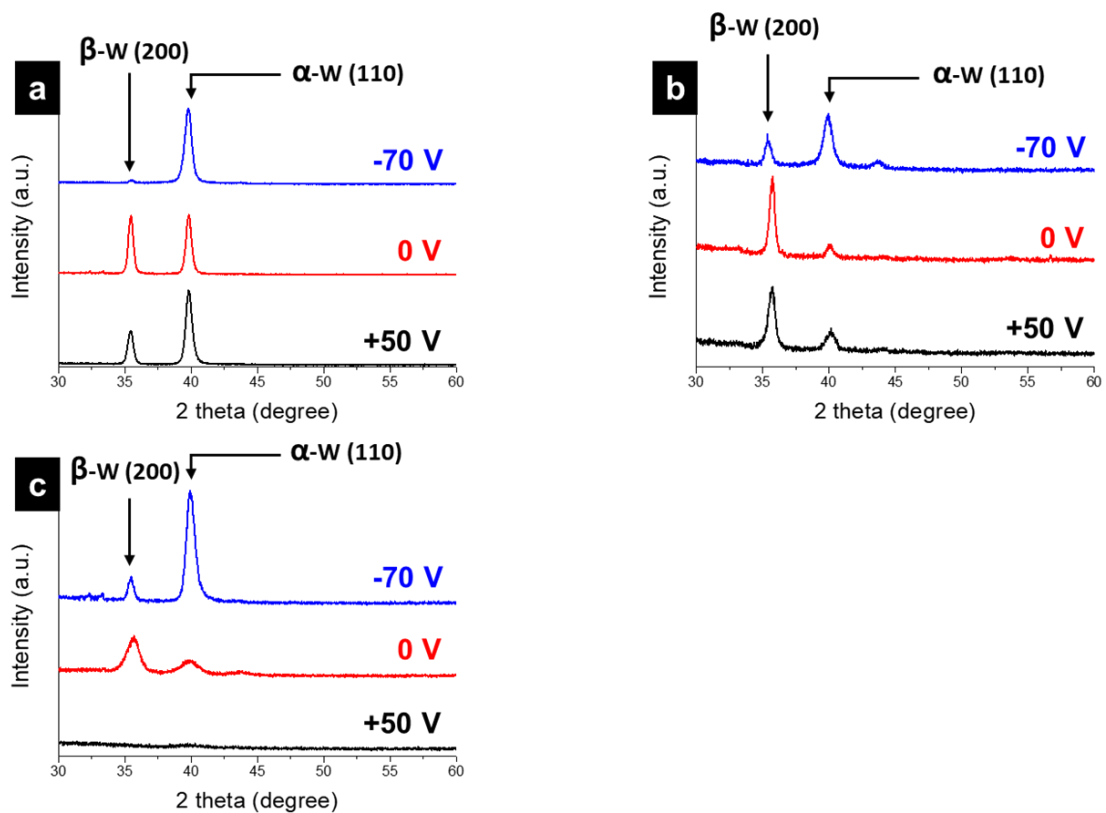


**Figure 4.6.** XRD of the films deposited by RF magnetron sputtering under (a) 5 mTorr, (b) 20 mTorr and (c) 80 mTorr.

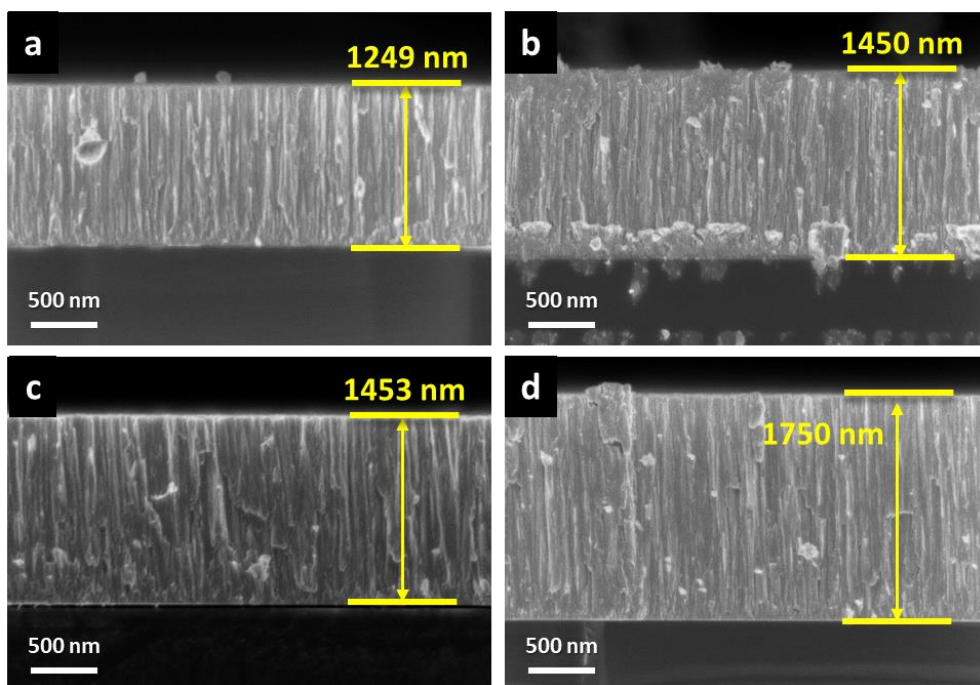


**Figure 4.7.** FESEM cross-section view images of the films deposited by HiPIMS under (a) 0.7 Pa and (b) 0.9 Pa, respectively, with 0.5 kW and under (c) 0.7 Pa and (d) 0.9 Pa, respectively, with 0.7 kW.

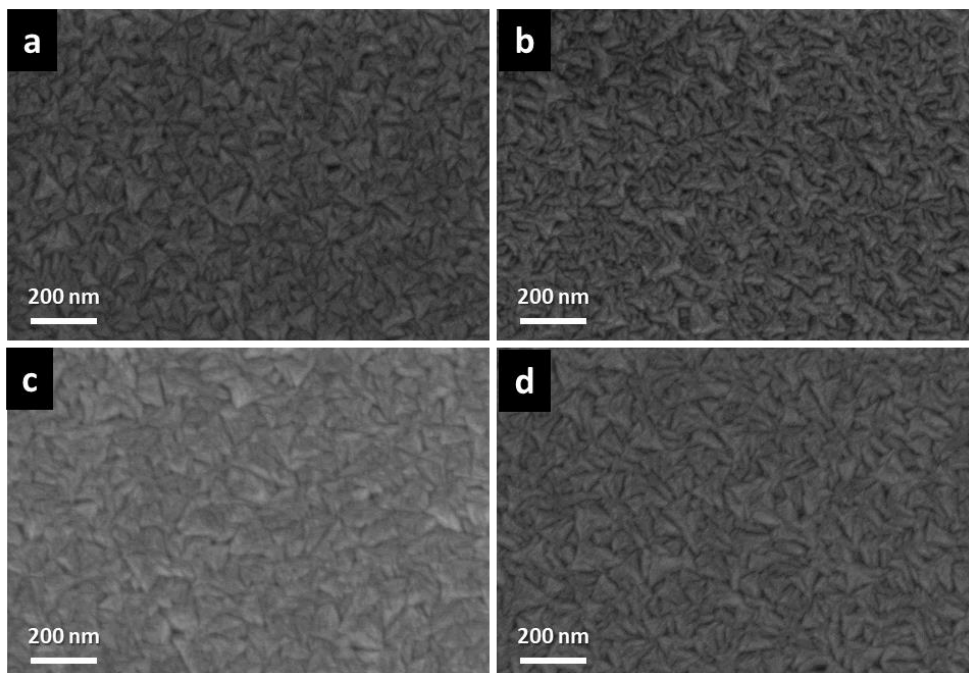


**Figure 4.8.** FESEM top view images of the films deposited by HiPIMS under (a) 0.7 Pa and (b) 0.9 Pa, respectively, with 0.5 kW and under (c) 0.7 Pa and (d) 0.9 Pa, respectively, with 0.7 kW.

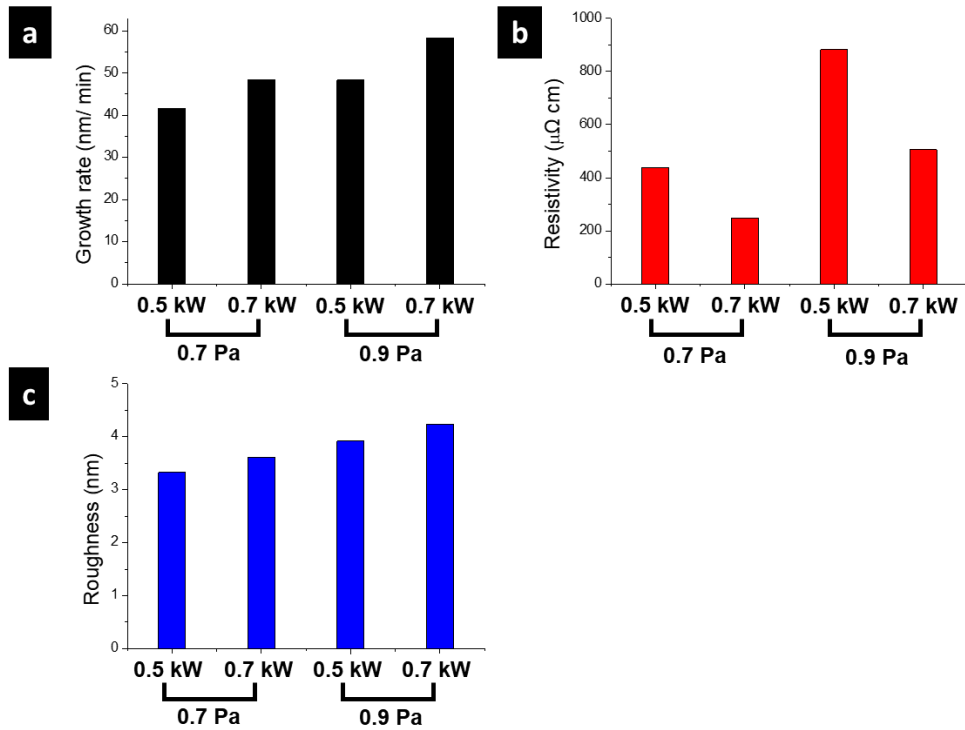


**Figure 4.9.** (a) growth rate, (b) resistivity and (c) roughness of the films deposited by HiPIMS

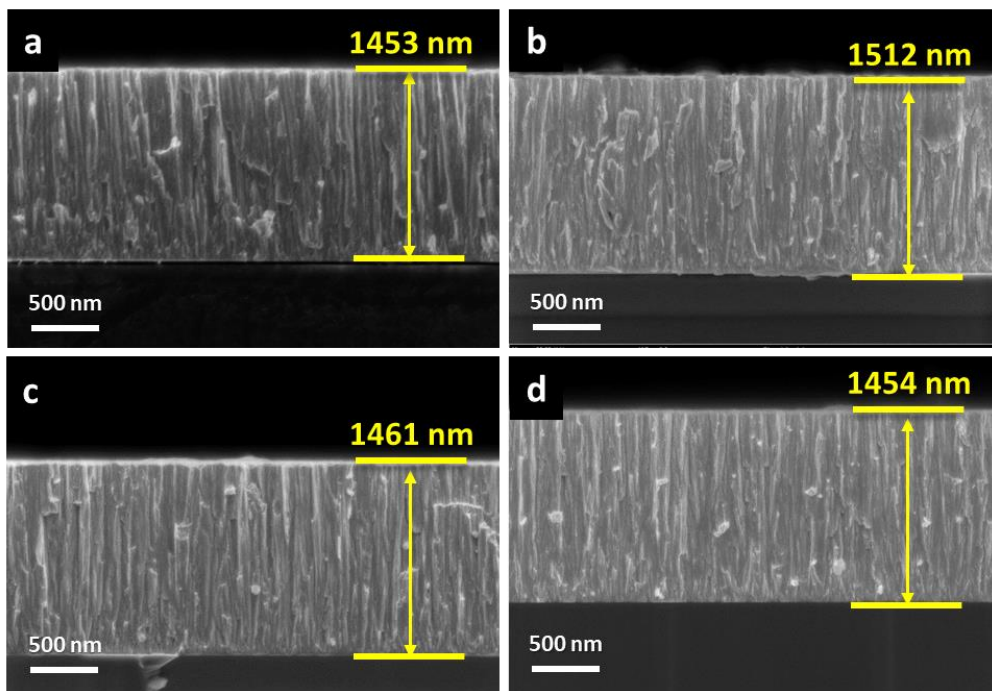


**Figure 4.10.** FESEM cross-section view images of the films deposited by HiPIMS with the substrate bias of (a) 0 V, (b)  $-10$  V, (c)  $-20$  V and (d)  $-30$  V under the pressure of 0.7 Pa with the average power of 0.7 kW.

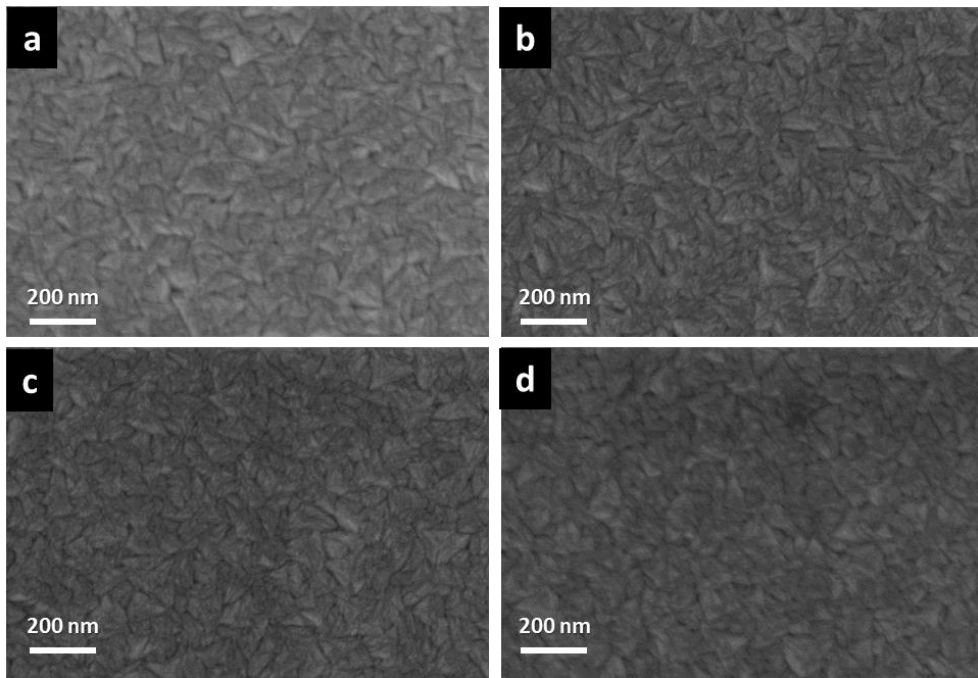


**Figure 4.11.** FESEM top view images of the films deposited by HiPIMS with the substrate bias of (a) 0 V, (b) -10 V, (c) -20 V and (d) -30 V under the pressure of 0.7 Pa with the average power of 0.7 kW.

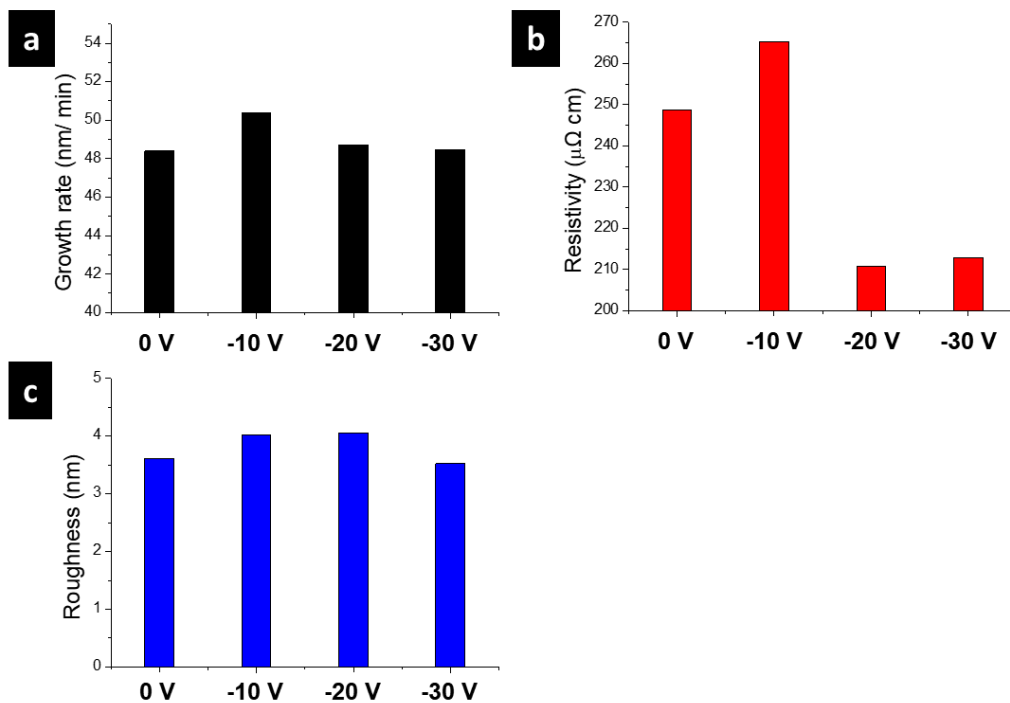


**Figure 4.12.** (a) growth rate, (b) resistivity and (c) roughness of the films deposited by HiPIMS with the substrate bias under the pressure of 0.7 Pa with the average power of 0.7 kW.

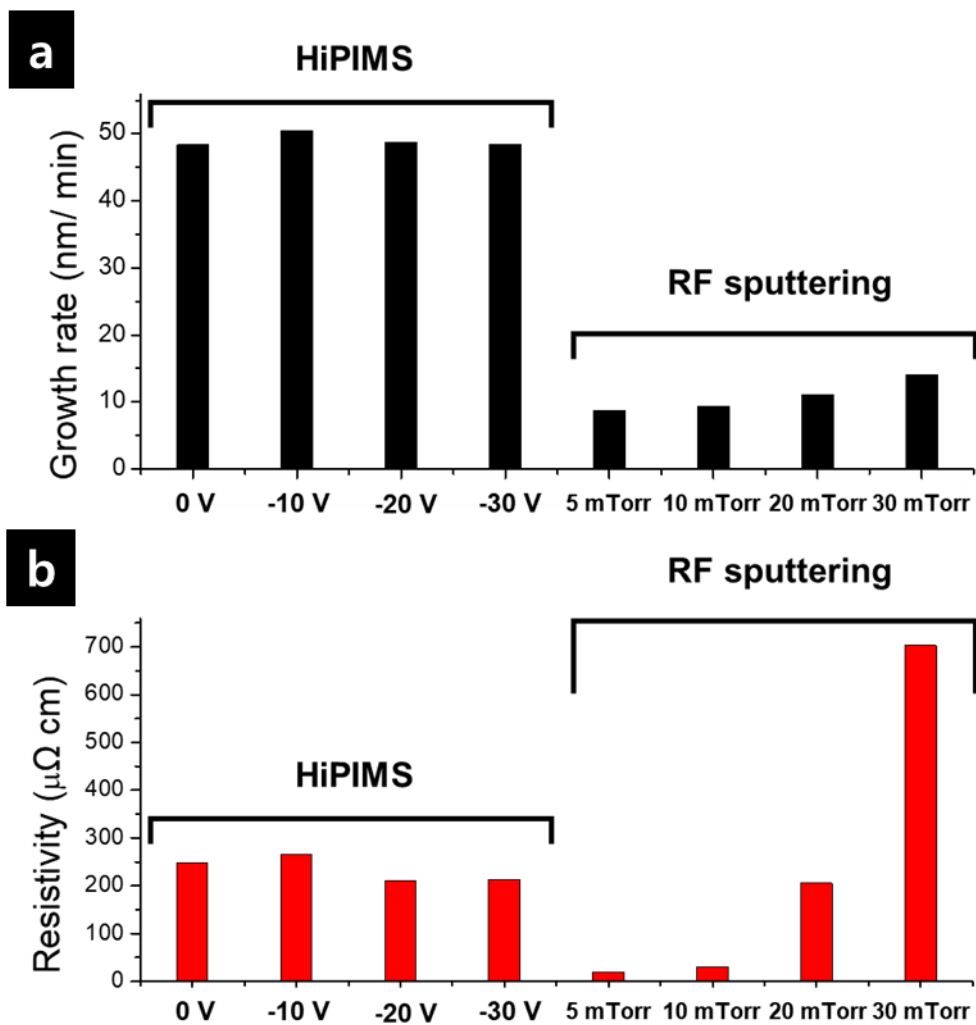
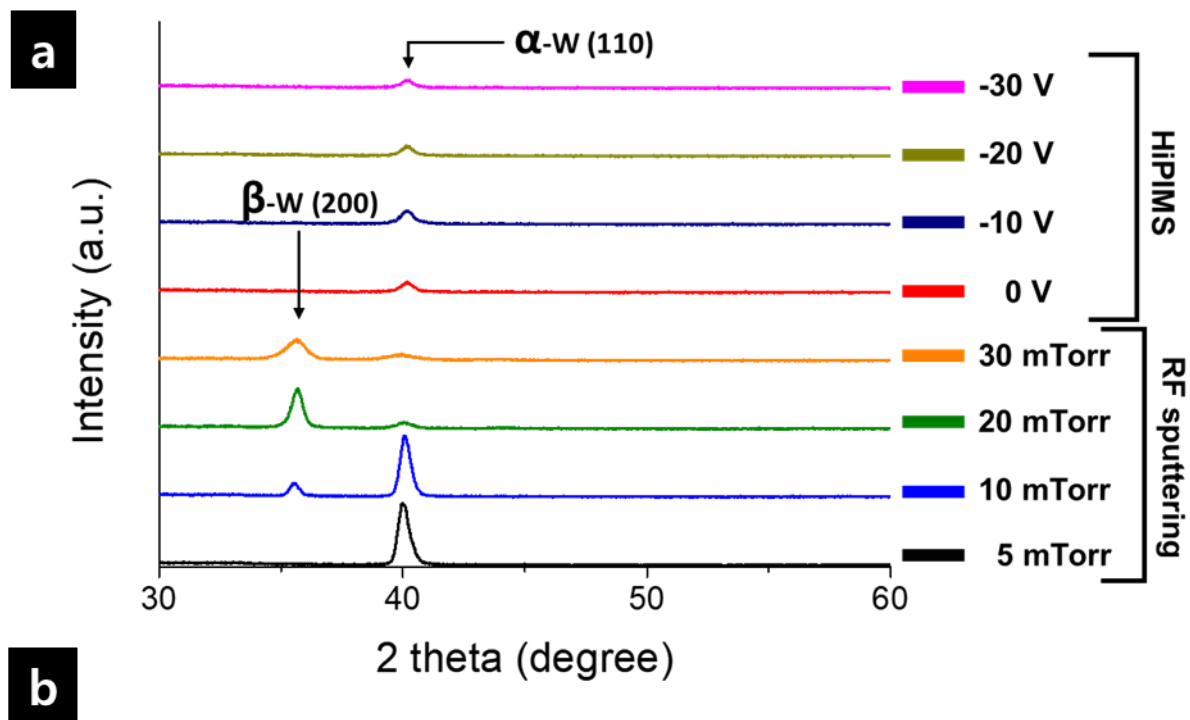


**Figure 4.13.** Comparison of (a) growth rate and (b) resistivity of the films deposited by HiPIMS and RF magnetron sputtering.





	HiPIMS				RF sputtering			
	0 V	-10 V	-20 V	-30 V	5 mTorr	10 mTorr	20 mTorr	30 mTorr
FWHM	0.535	0.552	0.57	0.508	0.531	0.501	0.635	1.055

**Figure 4.14.** Comparison of (a) XRD data and (b) FWHM of the films deposited by HiPIMS and RF magnetron sputtering.

# Bibliography

- [1] P. Hartman, Crystal Growth: An Introduction. 1973, Wiley, Amsterdam-London, 1974.
- [2] W.R. Wilcox, L.L. Regel, Handbook of crystal growth. Vol. 1: Fundamentals. a: thermodynamics and kinetics; b: transport and stability edited by DTJ Hurle, Acta Crystallographica Section A: Foundations of Crystallography 50(5) (1994) 652–653.
- [3] L. Boufendi, A. Plain, J.P. Blondeau, A. Bouchoule, C. Laure, M. Toogood, Measurements of particle size kinetics from nanometer to micrometer scale in a low-pressure argon-silane radio-frequency discharge, 60(2) (1992) 169–171.
- [4] A.A. Howling, L. Sansonnens, J.–L. Drier, C. Hollenstein, Negative hydrogenated silicon ionclusters as particle precursors in RF silane plasma deposition experiments, Journal of Physics D: Applied Physics 26(6) (1993) 1003.
- [5] S. Vepřek, O. Ambacher, W. Rieger, K. Schopper, M.G.J. Vepřek–Heijman, Clusters in a silane glow discharge: Mechanism of their formation and how to avoid them, MRS Online Proceedings Library Archive 297 (1993) 13–18.
- [6] A. Garscadden, B. Ganguly, P. Haaland, J. Williams, Overview of growth and behaviour of clusters and particles in plasmas, 3(3) (1994) 239.
- [7] E. Stoffels, W.W. Stoffels, G.M.W. Kroesen, F.J. De Hoog, Dust formation and charging in an Ar/SiH<sub>4</sub> radio-frequency discharge, Journal of Vacuum Science Technology A: Vacuum, Surfaces, Films 14(2) (1996) 556–561.

- [8] N.M. Hwang, D.Y. Yoon, Thermodynamic approach to the paradox of diamond formation with simultaneous graphite etching in the low pressure synthesis of diamond, *Journal of crystal growth* 160(1–2) (1996) 98–103.
- [9] N.M. Hwang, J.H. Hahn, D.Y. Yoon, Charged cluster model in the low pressure synthesis of diamond, *Journal of crystal growth* 162(1–2) (1996) 55–68.
- [10] N.M. Hwang, J.H. Hahn, D.Y. Yoon, Chemical potential of carbon in the low pressure synthesis of diamond, *Journal of crystal growth* 160(1–2) (1996) 87–97.
- [11] N.–M. Hwang, D.–Y. Kim, Charged clusters in thin film growth, *International materials reviews* 49(3–4) (2004) 171–190.
- [12] N.–M. Hwang, D.–K. Lee, Charged nanoparticles in thin film and nanostructure growth by chemical vapour deposition, *Journal of Physics D: Applied Physics* 43(48) (2010) 1–38.
- [13] J.–M. Huh, D.–Y. Yoon, D.–Y. Kim, N.–M. Hwang, Effect of substrate materials in the low–pressure synthesis of diamond: approach by theory of charged clusters, *Zeitschrift für Metallkunde* 96(3) (2005) 225–232.
- [14] C.–S. Kim, Y.–B. Chung, W.–K. Youn, N.–M. Hwang, Generation of charged nanoparticles during the synthesis of carbon nanotubes by chemical vapor deposition, *Carbon* 47(10) (2009) 2511–2518.
- [15] C.–S. Kim, Y.–B. Chung, W.–K. Youn, N.–M. Hwang, Generation of Charged Nanoparticles during Synthesis of ZnO Nanowires by Carbothermal Reduction, *Aerosol Science and Technology* 43(2) (2009) 120–125.
- [16] C.–S. Kim, W.–K. Youn, N.–M. Hwang, Generation of charged

- nanoparticles and their deposition during the synthesis of silicon thin films by chemical vapor deposition, *Journal of Applied Physics* 108(1) (2010) 1–6.
- [17] W.–K. Youn, S.–S. Lee, J.–Y. Lee, C.–S. Kim, N.–M. Hwang, S. Iijima, Comparison of the Deposition Behavior of Charged Silicon Nanoparticles between Floating and Grounded Substrates, *The Journal of Physical Chemistry C* 118(22) (2014) 11946–11953.
- [18] R.S. Wagner, W.C. Ellis, Vapor-liquid-solid mechanism of single crystal growth, *Applied physics letters* 4(5) (1964) 89–90.
- [19] R.Q. Zhang, Y. Lifshitz, S.T. Lee, Oxide-assisted growth of semiconducting nanowires, *Advanced Materials* 15(7-8) (2003) 635–640.
- [20] B.W. Clare, G. Talukder, P.J. Jennings, J.C.L. Cornish, G.T. Hefter, Effect of charge on bond strength in hydrogenated amorphous silicon, *Journal of computational chemistry* 15(6) (1994) 644–652.
- [21] C.T.T. GmbH, Low Pressure Chemical Vapor Deposition–Technology and Equipment.  
<https://www.crystec.com/klallpcvde.htm>.
- [22] C.T.T. GmbH, Plasma Enhanced Chemical Vapor Deposition, PECVD. <https://www.crystec.com/tridepe.htm>.
- [23] J. Tavares, E.J. Swanson, S. Coulombe, Plasma synthesis of coated metal nanoparticles with surface properties tailored for dispersion, *Plasma Processes Polymers* 5(8) (2008) 759–769.
- [24] R.E.I. Schropp, B. Stannowski, A.M. Brockhoff, P.A.T.T. Van Veenendaal, J. Rath, Hot wire CVD of heterogeneous and

- polycrystalline silicon semiconducting thin films for application in thin film transistors and solar cells, *Materials Physics Mechanics* 1 (2000) 73–82.
- [25] K.K.S. Lau, J.A. Caulfield, K.K. Gleason, Structure and morphology of fluorocarbon films grown by hot filament chemical vapor deposition, *Chemistry of Materials* 12(10) (2000) 3032–3037.
- [26] C.A.D. Dion, J.R. Tavares, Photo-initiated chemical vapor deposition as a scalable particle functionalization technology (a practical review), *Powder technology* 239 (2013) 484–491.
- [27] N. Selvakumar, H.C. Barshilia, Review of physical vapor deposited (PVD) spectrally selective coatings for mid-and high-temperature solar thermal applications, *Solar energy materials solar cells* 98 (2012) 1–23.
- [28] J.F. Hanlon, R.J. Kelsey, H. Forcinio, *Handbook of package engineering*, 3 ed., CRC press 1998.
- [29] E. Fortunato, P. Barquinha, R. Martins, Oxide semiconductor thin-film transistors: a review of recent advances, *Advanced materials* 24(22) (2012) 2945–2986.
- [30] Wikipedia, Sputter deposition.  
[https://en.wikipedia.org/wiki/Sputter\\_deposition](https://en.wikipedia.org/wiki/Sputter_deposition).
- [31] R.R. Boyer, An overview on the use of titanium in the aerospace industry, *Materials Science and Engineering A* 213 (1996) 103–114.
- [32] C.N. Elias, J.H.C. Lima, R. Valiev, M.A. Meyers, Biomedical Applications of Titanium and its Alloys, *JOM* (2008) 46–49.
- [33] L. Huang, B. Liu, Q. Zhu, S. Chen, M. Gao, F. Qin, D. Wang, Low

- resistance Ti Ohmic contacts to 4H-SiC by reducing barrier heights without high temperature annealing, *Applied Physics Letters* 100(26) (2012) 1–4.
- [34] M. Kaur, K. Singh, Review on titanium and titanium based alloys as biomaterials for orthopaedic applications, *Materials Science & Engineering C* 102 (2019) 844–862.
- [35] M. Suzuki, T. Kawakami, T. Arai, S. Kobayashi, Y. Koide, T. Uemura, N. Shibata, M. Murakami, Low-resistance Ta/Ti Ohmic contacts for p-type GaN, *Applied Physics Letters* 74(2) (1999) 275–277.
- [36] C. Ting, M. Wittmer, The use of titanium-based contact barrier layers in silicon technology, *Thin Solid Films* 96 (1982) 327–345.
- [37] V. Chawla, R. Jayaganthan, A.K. Chawla, R. Chandra, Morphological study of magnetron sputtered Ti thin films on silicon substrate, *Materials Chemistry and Physics* 111(2–3) (2008) 414–418.
- [38] V. Chawla, R. Jayaganthan, A.K. Chawla, R. Chandra, Microstructural characterizations of magnetron sputtered Ti films on glass substrate, *Journal of Materials Processing Technology* 209(7) (2009) 3444–3451.
- [39] A.Y. Chen, Y. Bu, Y.T. Tang, Y. Wang, F. Liu, X.F. Xie, J.F. Gu, Deposition-rate dependence of orientation growth and crystallization of Ti thin films prepared by magnetron sputtering, *Thin Solid Films* 574 (2015) 71–77.
- [40] J.B.O. Gonzalo F. Iriarte, Jorgen Westlinder, Fredrik Engelmark, Ilia V. Katardjiev, Synthesis of C-Axis-Oriented AlN Thin Films on high-conducting layers\_Al, Mo, Ti, TiN, and Ni, *ieee transactions on ultrasonics, ferroelectrics, and frequency control*

52(7) (2005) 1170–1174.

- [41] Y.L. Jeyachandran, B. Karunakaran, S.K. Narayandass, D. Mangalaraj, The effect of thickness on the properties of titanium films deposited by dc magnetron sputtering, *Materials Science and Engineering: A* 458(1–2) (2007) 361–365.
- [42] J.H. Kwon, D.Y. Kim, K.–S. Kim, N.–M. Hwang, Preparation of Highly (002) Oriented Ti Films on a Floating Si (100) Substrate by RF Magnetron Sputtering, *Electronic Materials Letters* (2019).
- [43] N. Muslim, Y.W. Soon, C.M. Lim, Y.N. Voo, Influence of sputtering power on properties of titanium thin films deposited by RF magnetron sputtering, *ARPJ Journal of Engineering and Applied Sciences* 10(16) (2015) 7148–7189.
- [44] J. Aizenberg, P.V. Braun, P. Wiltzius, Patterned Colloidal Deposition Controlled by Electrostatic and Capillary Forces, *PHYSICAL REVIEW LETTERS* 84(13) (2000) 2997–3000.
- [45] A. Demortiere, A. Snezhko, M.V. Sapozhnikov, N. Becker, T. Proslier, I.S. Aranson, Self-assembled tunable networks of sticky colloidal particles, *Nat Commun* 5(3117) (2014) 1–7.
- [46] J.A. Ferrar, M.J. Solomon, Kinetics of colloidal deposition, assembly, and crystallization in steady electric fields, *Soft Matter* 11 (2015) 3599–3611.
- [47] B. Sadri, D. Pernitsky, M. Sadrzadeh, Aggregation and deposition of colloidal particles: Effect of surface properties of collector beads, *Colloids and Surfaces A: Physicochemical and Engineering Aspects* 530 (2017) 46–52.
- [48] Z. Wang, B. He, G. Xu, G. Wang, J. Wang, Y. Feng, D. Su, B. Chen, H. Li, Z. Wu, H. Zhang, L. Shao, H. Chen, Transformable masks for colloidal nanosynthesis, *Nat Commun* 9(563) (2018) 1–9.

- [49] J.-S. Jung, N.-M. Hwang, Non-Classical Crystallization of Thin Films and Nanostructures in CVD Process, in: S. Neralla (Ed.), Chemical Vapor Deposition –Recent Advances and Applications in Optical, Solar Cells and Solid State Devices, InTech, Janeza Trdine 9, 51000 Rijeka, Croatia, 2016, pp. 23–67.
- [50] S.-S. Lee, C.-S. Kim, N.-M. Hwang, Generation of Charged Nanoparticles During the Synthesis of GaN Nanostructures by Atmospheric-Pressure Chemical Vapor Deposition, *Aerosol Science and Technology* 46(10) (2012) 1100–1108.
- [51] N.-M. Hwang, Non-classical crystallization of thin films and nanostructures in CVD and PVD processes, Springer 2016.
- [52] I.-D. Jeon, M.C. Barnes, D.-Y. Kim, N.-M. Hwang, Origin of positive charging of nanometer-sized clusters generated during thermal evaporation of copper, *Journal of Crystal Growth* 247 (2003) 623–630.
- [53] J.-S. Jung, S.-H. Lee, D.-S. Kim, K.-S. Kim, S.-W. Park, N.-M. Hwang, Non-classical crystallization of silicon thin films during hot wire chemical vapor deposition, *Journal of Crystal Growth* 458 (2017) 8–15.
- [54] D.-S. Kim, N.-M. Hwang, Synthesis of nanostructures using charged nanoparticles spontaneously generated in the gas phase during chemical vapor deposition, *Journal of Physics D: Applied Physics* 51(46) (2018) 1–23.
- [55] J.-W. Park, K.-S. Kim, N.-M. Hwang, Gas phase generation of diamond nanoparticles in the hot filament chemical vapor deposition reactor, *Carbon* 106 (2016) 289–294.
- [56] S.-H. Park, J.-W. Park, S.-M. Yang, K.-H. Kim, N.-M. Hwang,



- Effect of Electric Bias on the Deposition Behavior of ZnO Nanostructures in the Chemical Vapor Deposition Process, The Journal of Physical Chemistry C 119 (2015) 25047–25052.
- [57] W.-K. Youn, C.-S. Kim, J.-Y. Lee, S.-S. Lee, N.-M. Hwang, Generation of Charged Nanoparticles and Their Deposition Behavior under Alternating Electric Bias during Chemical Vapor Deposition of Silicon, The Journal of Physical Chemistry C 116 (2012) 25157–25163.
- [58] S.-W. Park, J.-S. Jung, K.-S. Kim, K.-H. Kim, N.-M. Hwang, Effect of Bias Applied to the Substrate on the Low Temperature Growth of Silicon Epitaxial Films during RF-PECVD, Crystal Growth & Design 18(10) (2018) 5816–5823.
- [59] S.-W. Yoo, S.-J. You, J.-H. Kim, D.-J. Seong, B.-H. Seo, N.-M. Hwang, Effect of substrate bias on deposition behaviour of charged silicon nanoparticles in ICP-CVD process, Journal of Physics D: Applied Physics 50(3) (2017) 1–9.
- [60] B.B. Sahu, W. Long, J.G. Han, Highly conductive flexible ultra thin ITO nanoclusters prepared by 3-D confined magnetron sputtering at a low temperature, Scripta Materialia 149 (2018) 98–102.
- [61] K. Hayasaki, Y. Takamura, N. Yamaguchi, K. Terashima, T. Yoshida, Scanning tunneling microscopy of epitaxial YBa<sub>2</sub>Cu<sub>3</sub>O<sub>7-x</sub> films prepared by thermal plasma flash evaporation method, Journal of Applied Physics 81(3) (1997) 1222–1226.
- [62] V.A. Matveev, N.K. Pleshanov, A.P. Bulkin, V.G. Syromyatnikov, The study of the oxidation of thin Ti films by neutron reflectometry, Journal of Physics: Conference Series 340(1)

(2012) 1–4.

- [63] T. Miyoshi, Y. Haga, O. Nittono, Microstructure and preferred orientation in pure titanium films deposited by two-facing-target-type DC sputtering, *Thin Solid Film* 281 (1996) 128–131.
- [64] M. Audronis, V. Bellido-Gonzalez, The effect of Ti sputter target oxidation level on reactive High Power Impulse Magnetron Sputtering process behavior, *Surf. Coat. Technol.* 205 (2011) S322–S325
- [65] B. Wu, Y. Yu, J. Wu, I. Shchelkanov, D.N. Ruzic, N. Huang, Y. Leng, Tailoring of titanium thin film properties in high power pulsed magnetron sputtering, *Vacuum* 150 (2018) 144–154
- [66] S. Ghasemi, P. Seyfi, A. Farhadizadeh, H. Ghomi, The experimental approach into the influence of external inductance on the discharge characteristic of HiPIMS, *J. Theor. Appl. Phys.* 13, (2019) 289–297
- [67] D. Kim, D.-Y. Kim, J.-H. Kwon, K.-S. Kim, N.-M. Hwang, Generation of Charged SiC Nanoparticles During HWCVD Process, *Electron. Mater. Lett.* 16 (2020) 498–505
- [68] G.-S. Jang, D.-Y. Kim, N.-M. Hwang, The Effect of Charged Ag Nanoparticles on Thin Film Growth during DC Magnetron Sputtering, *Coatings* 10(8) (2020) 736
- [69] J.-H. Kwon, D.-Y. Kim, N.-M. Hwang, Generation of Charged Ti Nanoparticles and Their Deposition Behavior with a Substrate Bias during RF Magnetron Sputtering, *Coatings.* 10(5) (2020) 443
- [70] B.N. Chapman, *Glow Discharge Processes: Sputtering and Plasma Etching*; Wiley: New York, NY, USA, 1980; pp. 1–406, ISBN 978-04-710-7828-9.
- [71] O. Briot, M. Moret, C. Barbier, A. Tiberj, H. Peyre, A. Sagna, S. Contreras, Optimization of the properties of the molybdenum back

- contact deposited by radiofrequency sputtering for  $\text{Cu}(\text{In}_{1-x}\text{Ga}_x)\text{Se}_2$  solar cells, *Sol. Energy Mater. Sol. Cells* 174 (2018) 418–422
- [72] V. Kampylafka, A. Kostopoulos, M. Modreanu, M. Schmidt, E. Gagaoudakis, K. Tsagaraki, V. Kontomitrou, G. Konstantinidis, G. Deligeorgis, G. Kiriakidis et al. Long-term stability of transparent n/p ZnO homojunctions grown by rf-sputtering at room-temperature, *J. Mater.* 5 (2019) 428–435
- [73] M. Acosta, R.A. Méndez, I. Riech, M. Rodríguez-Pérez, G. Rodríguez-Gattorno, Structural, optical and photoelectrochemical properties of tungsten oxide thin films grown by non-reactive RF-sputtering, *Superlattices Microstruct.* 127 (2019) 123–127

## 국 문 초 록

비 고전적 결정화는 화학 기상 증착에서 광범위하게 연구되어 왔으며, 물리적 기상 증착에서 이를 연구할 필요성이 있다. 따라서 물리적 기상 증착 공정 중 하나인, RF 스퍼터링 공정에서 하전된 나노 입자의 생성을 확인하고 이들이 박막 증착에 미치는 영향, 그리고 압력에 따른 거동 변화에 대해 연구하였다. 우선, 티타늄 타겟을 사용하였으며, 티타늄 나노 입자는 비정질 탄소 멤브레인을 공정 중 짧은 시간 동안 노출시켜 포집되었다. 투과 전자 현미경으로 관찰한 결과, 약 4 nm 크기의 나노 입자가 관찰되었고 티타늄 나노 입자로 확인되었다. 또한, 멤브레인에 -70, 0, +5, +15 및 + 30 V의 바이어스를 가하며 하전 가능성을 조사하였다. 티타늄 나노 입자의 개수 농도는 음의 바이어스가 증가함에 따라 증가한 반면, 양의 바이어스를 가했을 경우 감소하였다. 따라서 이 티타늄 나노 입자들이 양전하를 띠고 있음을 알 수 있었다. 동일한 조건과 실험 조건에서 실리콘 기판 위에 티타늄 박막을 증착하였으며, 기판에 -70, 0, +30 V의 바이어스를 가해 주었다. 박막을 투과 전자 현미경, 전계 방출 주사 전자 현미경, X-선 회절, X-선 반사율로 분석하였다. 그 결과, 0 V에서 증착된 박막과 비교하여, -70 V에서 증착된 박막이 가장 좋은 결정도, 증착 속도 및 밀도를 갖는 반면, +30 V에서 증착된 박막은 가장 낮은 결정도, 증착 속도 및 밀도를 보였다. 이 차이는 -70 V에서 증착된 박막의 경우 양으로 하전된 나노 입자를 끌어왔기 때문으로 보이며, +30 V에서 증착된 박막의 경우 하전된 나노 입자가 아닌 중성 입자들에 의한 증착

때문인 것으로 보인다. 즉, 박막의 품질 향상을 위해, 하전된 나노 입자의 개수 농도 조절이 필요함을 확인할 수 있다.

또한 압력이 티타늄 나노 입자의 생성에 미치는 영향과, 압력에 따른 박막 증착 거동 차이를 연구하였다. 앞선 실험과 마찬가지로 비정질 탄소 멤브레인을 이용하여 나노 입자를 포집하였다. 20 mTorr와 80 mTorr에서 멤브레인에  $-30, 0, +50$  V의 바이어스를 가하며 포집한 결과, 역시 양으로 하전된 티타늄 나노 입자가 관찰되었다. 바이어스에 따른 개수 농도 차이는 압력이 증가함에 따라 증가하였다. 이는 압력이 증가함에 따라 티타늄 나노 입자가 하전된 비율이 증가했음을 의미한다. 동일한 조건에서 티타늄 필름을 증착한 결과 역시, 압력이 증가함에 따라 바이어스에 따른 증착 속도 차이가 증가하였다. 즉, 높은 압력에서의 큰 증착 속도 차이와 높은 압력에서의 큰 나노 입자의 하전 비율이 일치한다.

이러한 이해를 바탕으로 텅스텐 박막의 저항을 감소시키는 연구를 진행하였다. 5 mTorr, 20 mTorr, 80 mTorr의 압력에서 실리콘 기판에  $-70, -30, -10, 0, +50$  V의 바이어스를 가하며 텅스텐 박막을 증착하였다. 기판에 음의 바이어스를 가한 경우 박막의 저항이 감소한 반면, 양의 바이어스를 가한 경우 박막의 저항이 증가하였다. 또한 앞선 실험에서 얻은 이해와 같이 저항에 대한 이러한 바이어스 효과는 압력이 증가함에 따라 더욱 커졌다. 이 차이는 기판에 가해진 바이어스에 따라 하전된 나노 입자의 개수 농도가 차이났기 때문일 것이다. 한편 이러한 관점에서 고출력 임펄스 마그네트론 스퍼터링 (HiPIMS)이 RF 스퍼터링에 비해 더 높은 이온화율을 가지므로 나노 입자의 하전을 더욱 유도할 수 있다. 비록 HiPIMS를 사용하여 증착한 텅스텐 박막이 RF

스퍼터링보다 높은 저항을 보였지만, 훨씬 높은 증착 속도를 나타내었다. 추후, HiPIMS의 공정 조건을 최적화하고 나노 입자의 하전을 유도할 수 있는 추가적인 장비를 도입한다면, 더욱 낮은 저항을 가진 박막을 높은 증착 속도로 얻을 수 있을 것이라 예상한다.